11 SCIENTIFIC HIGHLIGHT OF THE MONTH

Third-generation MTOs

O. K. Andersen, T. Saha-Dasgupta, S. Ezhov, L. Tsetseris, O. Jepsen,
R.W. Tank, C. Arcangeli, and G. Krier
Max-Planck Institute für Festkörperforschung, D-70569, Stuttgart, Germany

Abstract

The 3rd-generation muffin-tin orbital formalism is reviewed and illustrated by applications to tetrahedrally coordinated semiconductors and high-temperature superconductors.

Introduction

Muffin-tin orbitals (MTOs) have been used for a long time in *ab initio* calculations of the electronic structure of condensed matter. Over the years, several MTO-based methods have been developed. The ultimate aim is to find a generally applicable electronic-structure method which is *intelligible, fast,* and *accurate.* Our recent progress in that direction will be reported in the present Highlight.

In order to be *intelligible* an electronic-structure method should, in our opinion, employ a *minimal* and *flexible* basis of *short-ranged* orbitals. As an example, the method should be able to describe the valence electrons in *sp*-bonded materials using merely four short-ranged *s*- and *p*-orbitals per atom and, for insulating phases, using merely *occupied* orbitals such as bond orbitals. Another example is materials with strong electronic correlations. For such materials, one must first construct a realistic Hamiltonian, and this requires an accurate single-particle basis which can be partitioned into correlated and non-correlated orbitals, without introducing too many of the former. A flexible basis of short-ranged orbitals is thus asked for. The method should, in other words, enable the user to construct a first-principles, solvable Hamiltonian for the problem at hand.

Now, a small basis of short-ranged orbitals is a prerequisite for a method to be *fast,* but it may be a hindrance for the *accuracy,* because the orbitals of a smaller basis are in general more complicated than those of a larger basis.

Most other *ab initio* methods, such as plane-wave pseudopotential, LAPW, PAW, and LCAO methods, aim at *simulation,* and are therefore primarily *accurate* and *robust.* But they are neither fast nor intelligible in the above-mentioned sense, because they employ basis sets with about hundred functions per atom. *Understanding* is therefore attempted *after* the calculation, by means of projections onto *e.g.* charge densities, electron-localization functions (ELFs), partial waves, Wannier functions in case of insulators, a.s.o.

In this Highlight we start by explaining broadly what 3rd-generation MTOs are and, by the examples of diamond-structured Si and the CuBr - Ge series, demonstrate that they are intelligible and accurate.

Next, we sketch the formalism, which is essentially the multiple-scattering formalism of Korringa, Kohn, and Rostoker (KKR) [1] with the following three extensions: (1) Exact *screening* transformations are introduced to reduce the spatial range and the energy dependence -or the dimension- of the structure matrix. (2) The formalism is proved to hold for *overlapping* MT potentials, to leading order in the potential-overlap. (3) Energy-independent MTO basis sets are derived which span the solutions $\Psi_i(\mathbf{r})$ with energies ε_i of Schrödinger's equation to within errors proportional to $(\varepsilon_i - \epsilon_0)(\varepsilon_i - \epsilon_1)..(\varepsilon_i - \epsilon_N)$, where $\epsilon_0, \epsilon_1, ..., \epsilon_N$ is a chosen energy mesh. By virtue of the variational principle, the errors of the energies ε_i are then proportional to $(\varepsilon_i - \epsilon_0)^2(\varepsilon_i - \epsilon_1)^2..(\varepsilon_i - \epsilon_N)^2$. To work with a discrete energy mesh and divided, finite differences is far more flexible and accurate than working with a condensed mesh and energy derivatives, as was the case for the linear (N=1) MTO (LMTO) methods of the 1st- and 2nd-generation. Moreover, in those methods the partial waves inside the MT-spheres were treated to linear order, but the wave function in the interstitial was treated merely to zeroth order. For the MTOs of the 3rd-generation, the MT-spheres and the interstitial regions are treated on the same footing like in the KKR method, because only in that case is there an elegant and efficient way of treating downfolding and overlapping MT-potentials. This, however, causes the expansion energies ϵ_n to be *global* parameters, independent of the Rl-channel, and that is why we often need to go beyond *linear* methods. Descriptions of how we expand the charge density locally in screened spherical waves and of how the overlapping MT-potential, which defines the MTO basis set, is derived from the full potential, lie outside the scope of the present Highlight, but we refer to previous [2, 3, 4, 5] and coming [6] publications. Moreover, our production code for those parts of the new method is still under construction [7]. The overlapping-potential feature of the present formalism has been taken up also by Vitos et al. [8] in Green-function calculations for closely-packed alloys with the usual cell-projection technique for the charge density.

In the final section we demonstrate how 3rd-generation MTOs have been used to discover the material-dependent trend in the band structures of the hole-doped high-temperature superconductors and its correlation with the maximum T_c [9].

Most readers would presumably look at merely the first and the last sections, skipping the heavy middle part about the formalism. For the rare person who might want to know more, we refer to the original papers [2, 3, 4, 5, 10].

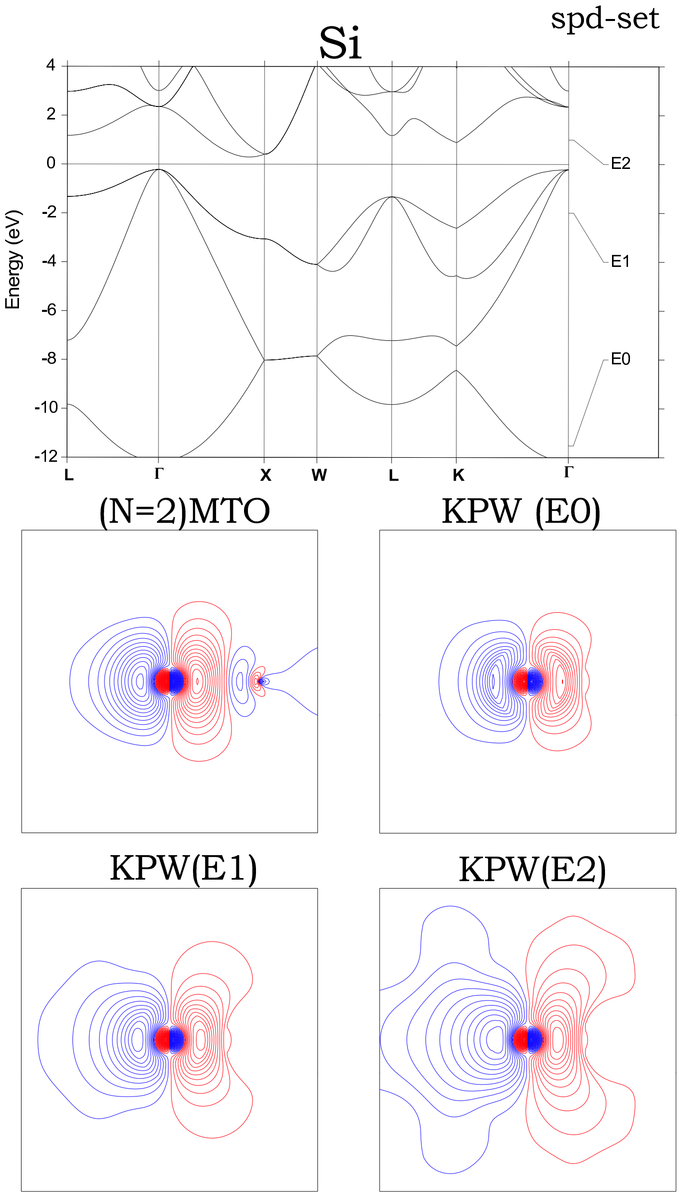

(N=2)MTO

KPW (E0)

KPW(E1)

KPW(E2)

Figure 1: Band structure of Si calculated with the Si *spd*-QMTO basis set corresponding to the energy mesh shown on the right-hand side. The contour plots show the Si *p* orbital pointing in the [111]-direction between two nearest neighbors in the $(1\bar{1}0)$-plane. Shown are the kinked partial waves (KPWs) at the three energies and the QMTO. The KPWs are normalized to one, times a cubic harmonics, at the central hard sphere [see Eqs. (14 and (21)]. The contours are the same in all plots. See text.

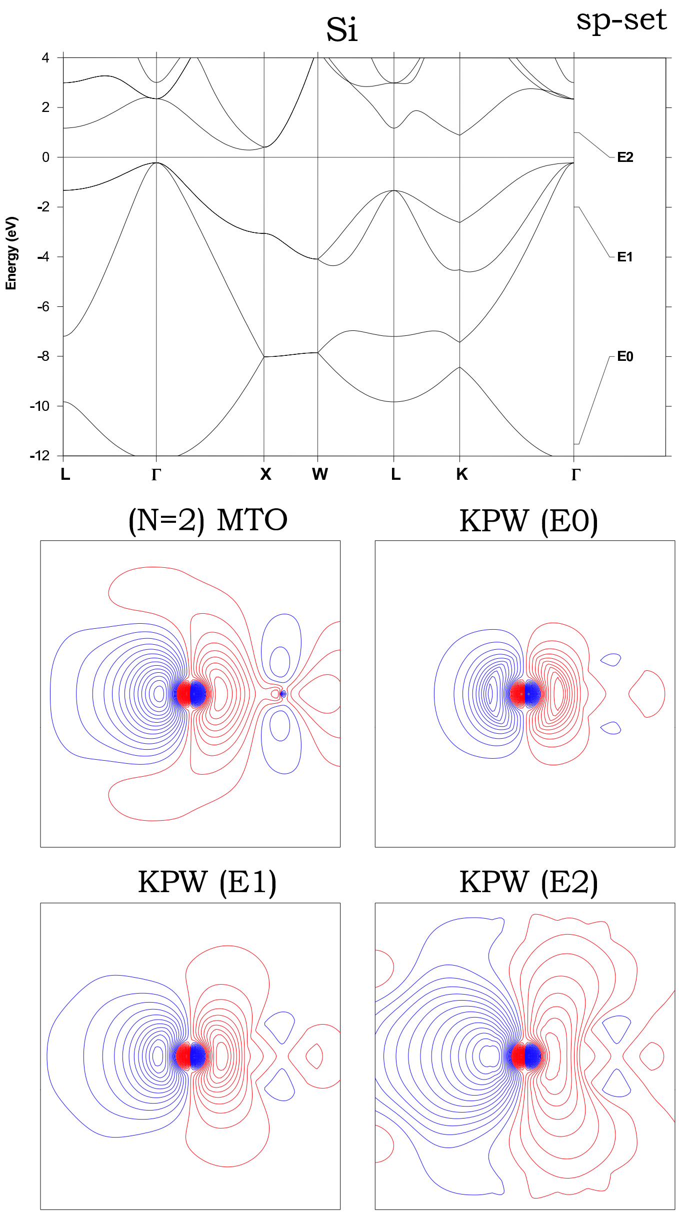

Figure 2: Same as Fig.1, but for the Si *sp*-set.

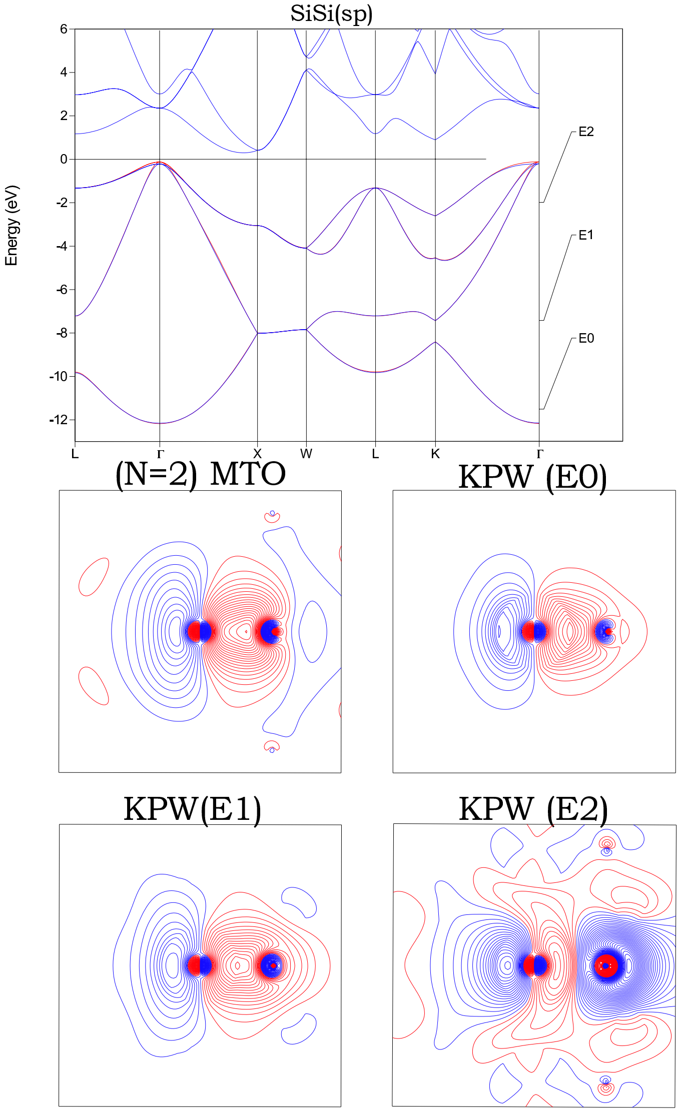

Figure 3: Same as Figs. 1-2, but for the Si(*sp*)Si-set with *sp*-QMTOs on merely every second Si atom, the one seen to the left in the figure. The red valence bands are obtained with this 'ionic' $Si^{4-}Si^{4+}$ basis. The blue, stippled bands are the ones from Fig. 1.

Illustrations for tetrahedrally-bonded semiconductors

At the top of Fig. 1 we show the LDA energy bands $\varepsilon_i(\mathbf{k})$ of Si in the diamond structure, calculated with the basis set of Si-centered *s*-, *p*-, and *d*-MTOs (9 orbitals/atom) for the energy mesh ϵ_0, ϵ_1, ϵ_2 indicated on the right-hand side. These bands have meV-accuracy for the MT-potential used for their construction, which in the present case was the standard all-electron, Si_2E_2 atomic-spheres potential. With three energy points, the MTOs are of order N=2, that is, they are *quadratic* MTOs, so-called QMTOs.

The *p*-QMTO pointing along [111], from one Si to its nearest neighbor, is shown in the $(1\bar{1}0)$-plane by the first contour plot. This orbital is localized and smooth with a few wiggles at the nearest neighbor. The remaining three contour plots show the major constituents of this p_{111}-QMTO: The p_{111}-*kinked partial wave* (KPW) at the central site for the three energies. In general, the NMTOs for the energy mesh $\epsilon_0, ..., \epsilon_N$ are superpositions:

$$\chi_{R'L'}^{(N)}(\mathbf{r}) = \sum_{n=0}^{N} \sum_{RL \in A} \phi_{RL}(\epsilon_n, \mathbf{r}) \; L_{nRL,R'L'}^{(N)}, \tag{1}$$

of the kinked partial waves, $\phi_{RL}(\varepsilon, \mathbf{r})$, at the $N+1$ points of the energy mesh. In the present case, the L=lm-summation is over the s-, p-, and d-KPWs, and the R-summation is over the Si sites, that is, over mainly the nearest neighbors, as a comparison between the contour plots of the QMTO and the KPWs should reveal. These RL-values, for which we have MTOs in the basis set, we call the *active* (A) ones.

A KPW is basically a *partial wave with a tail* joined continuously to it with a *kink* at a central, so-called hard sphere of radius a_R. This kink is seen in the contour plots, and most clearly for the lowest energy, ϵ_0. As usual, the partial wave $\varphi_{Rl}(\varepsilon, r_R) Y_L(\hat{\mathbf{r}}_R)$, where $r_R \equiv |\mathbf{r} - \mathbf{R}|$ and $\hat{\mathbf{r}}_R \equiv \widehat{\mathbf{r} - \mathbf{R}}$, is a product of a spherical (or cubic) harmonic and a regular solution with energy ε of the radial Schrödinger equation,

$$-\left[r\varphi_{Rl}(\varepsilon, r)\right]'' = \left[\varepsilon - v_R(r) - l(l+1)/r^2\right] r\varphi_{Rl}(\varepsilon, r), \tag{2}$$

for the potential $v_R(r)$ of the MT-well at $\mathbf{R}$. The tail of the kinked partial wave is a so-called *screened spherical wave* (SSW), $\psi_{RL}(\varepsilon, \mathbf{r})$, which is essentially the solution with energy ε of the wave equation in the interstitial between the hard spheres, $-\Delta\psi(\varepsilon, \mathbf{r}) = \varepsilon\psi(\varepsilon, \mathbf{r})$, satisfying the boundary condition that, independent of the energy, $\psi_{RL}(\varepsilon, \mathbf{r})$ go to $Y_L(\hat{\mathbf{r}}_R)$ at the central hard sphere and to *zero* (with a kink) at all other hard spheres. It is this latter confinement, easily recognized in the KPW contour plots, particularly at the highest energy ϵ_2, which makes the KPW localized, when the energy is not too high. At the same time, it makes the KPW have pure L-character at the central sphere only, because outside it is influenced by the hard spheres centered at the neighbors. The default value of the hard-sphere radii is 90 per cent of the covalent, atomic, or ionic radius, whichever is appropriate.

The kinked partial wave thus has a kink, not only at its own, but also at the neighboring hard spheres, inside which it essentially vanishes. 'Essentially' because the above-mentioned boundary condition only applies to the active components of the spherical-harmonics expansions of the SSW on the hard spheres. For the *passive* components, in the present case the Si f- and higher components, as well as all components on empty (E) spheres, the SSW equals the corresponding partial-wave solution of Schrödinger's equation throughout the MT-sphere. The small bump seen in the lowest contour along the [111]-direction is caused by the slight f-character on the nearest neighbor.

In the valence and lowest conduction bands of Si there are only s- and p-, but no d-electrons. We should therefore be able to use a basis with only Si s- and p-MTOs, that is, with only 4 orbitals per atom. In the language used above, we thus let the Si s- and p-partial waves remain active, while the Si d-waves are included among the passive ones, *i.e.* those 'folded down' into the SSW-tails of the active KPWs. The results for the bands and the p_{111}-QMTO are shown in Fig. 2. These bands are indistinguishable from those obtained with the Si *spd*-set, on the scale of the figure, although between the energies of the mesh, the bands obtained with the *sp*-set do lie slightly above those obtained with the *spd*-set. However, by making the mesh denser (increasing N), the accuracy can be increased arbitrarily. The KPW of the *sp*-set is seen to

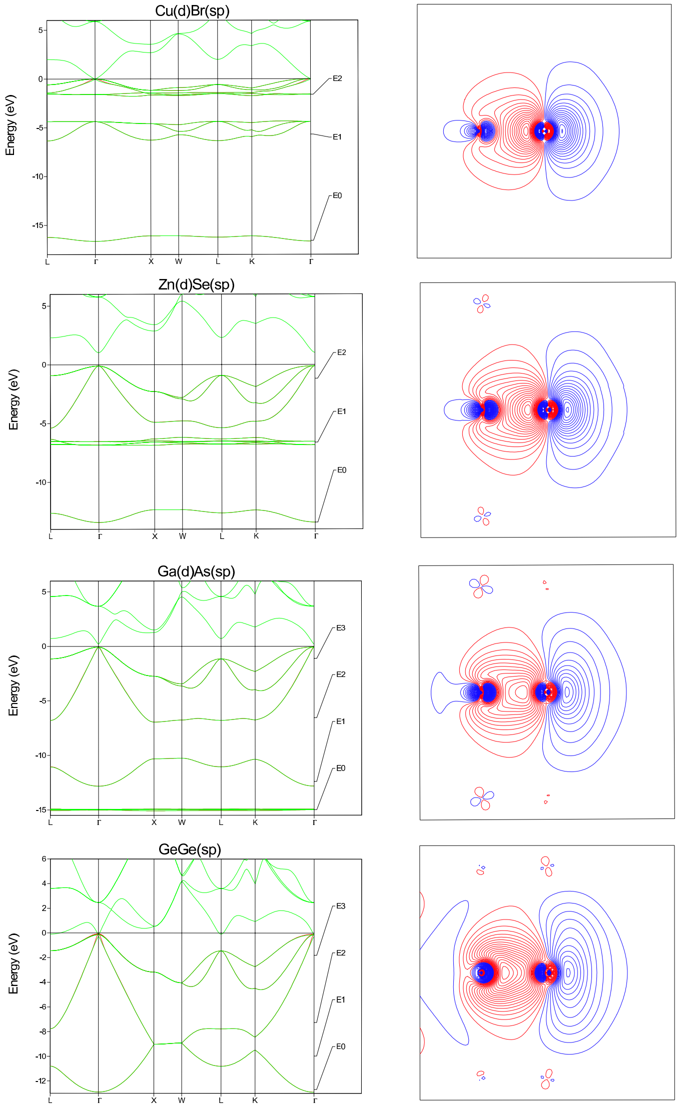

Figure 4: Valence bands (red) of the series CuBr – Ge, calculated with the ionic basis sets where the *sp*-MTOs are on the anion and, except for Ge, the *d*-MTOs are on the cation. The contour plots show the p_{111}-MTO on the anion (the atom to the right). From top to bottom, the ionicity decreases and the covalency increases.

have *d*-character on the nearest Si neighbor, and the QMTO and the KPW, particularly the one at the highest energy, are seen to be somewhat less localized than those for the *spd*-set.

It is even possible to construct an arbitrarily accurate MTO-basis which spans merely the *occupied* orbitals, that is, which spans the valence band with a basis of merely 2 orbitals per atom. An advantage of this is that the sum of the one-electron energies might be calculated in real space, without diagonalization, as the trace of the Hamiltonian, using the MTO orthonormalization procedure described in Sect. 5 of Ref. [5]. This is a method where the amount of computation increases merely linearly with the size of the system (or cell), a so-called *order*-N *method* (Here, N refers to the number of atoms in the system, not the order N of the MTOs). For covalent semiconductors like Si it is customary to take the valence-band orbitals as the bond-orbitals, which are the bonding linear combinations of the directed sp^3-hybrids of orthonormal MTOs. It is, however, far simpler and more general, *e.g.* not limited to elemental semiconductors and tetrahedral structures, to take the valence-band orbitals as the *s*- and *p*-MTOs on *every second* Si atom, all partial waves on the nearest neighbors being downfolded. This corresponds to an *ionic* description, $\mathrm{Si}^{4-}\mathrm{Si}^{4+}$. As Fig. 3 shows, this QMTO-set describes merely the valence band and it does so surprisingly well, considering the fact that the two silicons are treated differently so that the degeneracy along the XW-line is slightly broken. The error between the energy points is proportional to $[\varepsilon_i(\mathbf{k})-\epsilon_0][\varepsilon_i(\mathbf{k})-\epsilon_1][\varepsilon_i(\mathbf{k})-\epsilon_2]$, like for the basis with 4 orbitals per atom shown in Fig. 2 because we used QMTOs in both cases, but the prefactors are larger for the smaller basis. This comes from the longer range and the concomitant stronger energy dependence of the KPWs as the number of active channels decreases. However, by making the mesh finer, the errors can be made arbitrarily small. In the present case, the basis with 2 *cubic* MTOs (CMTOs) per atom turns out to yield energies with about the same accuracy as the basis with 4 QMTOs per atom. After orthonormalization of this ionic valence-band set, the sum of the one-electron energies may be calculated as the trace of the Hamiltonian. The directed sp^3-hybrids formed from these orbitals actually look like bond orbitals. Since the ionic Si(*sp*)Si-set gives the occupied states in diamond-structured Si with arbitrary accuracy, the same procedure with the *sp*-orbitals placed exclusively on the *anion* (but with the *d*-orbitals on the cation), will of course work for any IV-IV, III-V, II-VI, and I-VII semiconductor and insulator. This is illustrated in Fig. 4. Such *ionic* MTO *basis sets* which 'automatically' span the occupied, and no further, states of any non-metal could make density-functional molecular-dynamics calculations highly efficient for such systems.

As an example of a minimal set spanning all states in a *wide* energy range, we show in Fig. 5 for GaAs the LDA valence and conduction bands, 18 of which fall in the 35 eV-range displayed. The dotted bands were calculated variationally using a basis of Ga *spd*- and As *spdf*-QMTOs. The good accuracy obtained with this basis of merely 25 orbitals per cell demonstrates the power of the NMTO method. Note that *no* principal quantum numbers were needed, even for this large energy range which includes the Ga 3*d* semi-core band at -15 eV. This NMTO representation should be useful for computing excited-state properties, *e.g.* with the GW method [11]. For calculating x-ray dichroism spectra of magnetic materials, a relativistic spin-polarized version of the NMTO method has been developed [12].

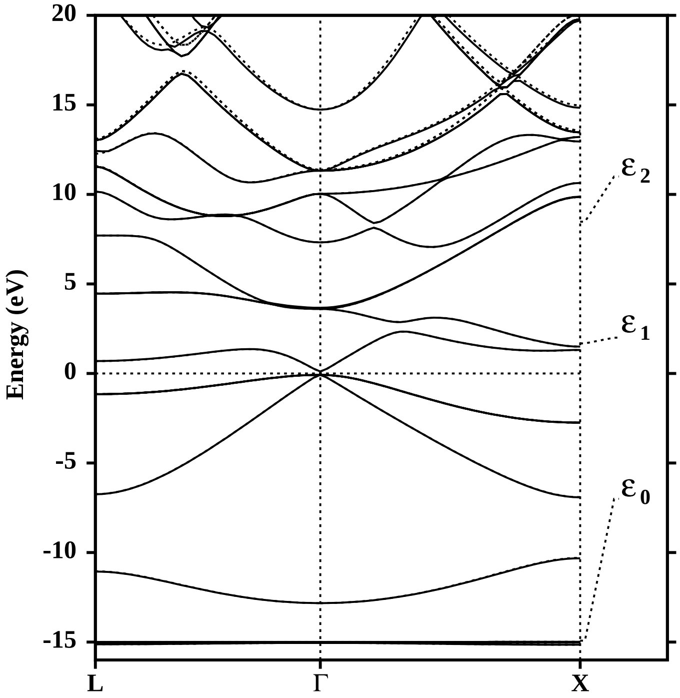

Figure 5: Band structure of GaAs over a wide energy range, calculated with the QMTO method and the energy mesh indicated on the right-hand side (dashed), compared with the exact result (solid).

Formalism

In this section we review the formalism behind the illustrations in Figs. 1-5. We first consider the tail-functions, the screened spherical waves.

Screened spherical waves (SSWs)

The screened spherical wave at site R' and with angular momentum L' at the own hard sphere is a linear combination of *bare* spherical waves:

$$n^{\alpha}_{R'L'}(\varepsilon,\mathbf{r}) = \sum_{RL\in A} n_l(\kappa r_R)\, Y_L(\hat{\mathbf{r}}_R)\; X^{\alpha}_{RL,R'L'}(\varepsilon) \equiv \sum_{RL\in A} n^{0}_{RL}(\varepsilon,\mathbf{r})\; X^{\alpha}_{RL,R'L'}(\varepsilon)\,, \tag{3}$$

whose radial parts we have here written as spherical Neumann functions, rather than decaying Hankel functions, because we want to keep the notation of scattering theory although the energies ($\kappa^2 \equiv \varepsilon$) of the valence band are mostly negative when we use overlapping MT-spheres. The screening transformation $X^{\alpha}(\varepsilon)$ is determined by the hard-sphere boundary condition and the superscripts α refer to the choice of hard spheres, as well as the normalization as will later become evident. Finally, we have written n^{α} instead of ψ^{α}, because in (3) we have not yet truncated the active components and augmented the passive ones. In order to determine $X^{\alpha}(\varepsilon)$ in such a way that $n^{\alpha}(\varepsilon,\mathbf{r})$ fits the boundary conditions, we need to expand $n^{\alpha}_{R'L'}(\varepsilon,\mathbf{r})$ in spherical-harmonics around all sites. For this, we have the well-known expansion:

$$n_l(\kappa r_R)\, Y_L(\hat{\mathbf{r}}_R) = \sum_{\bar{L}} j_{\bar{l}}(\kappa r_{\bar{R}})\, Y_{\bar{L}}(\hat{\mathbf{r}}_{\bar{R}})\; \kappa^{-1} B^{0}_{\bar{R}\bar{L},RL}(\varepsilon)\,, \tag{4}$$

of the *bare* spherical wave at site R in spherical harmonics around another site $\bar{R}$. The expansion coefficients are spherical Bessel functions times

$$\kappa^{-1} B^{0}_{\bar{R}\bar{L},RL}\left(\varepsilon\right) \;\equiv\; \sum_{l'} 4\pi\, i^{-l+\bar{l}-l'} C_{L\bar{L}l'}\, n_{l'}\left(\kappa\left|\mathbf{R}-\bar{\mathbf{R}}\right|\right) Y^{*}_{l'(\bar{m}-m)}\left(\widehat{\mathbf{R}-\bar{\mathbf{R}}}\right), \tag{5}$$

where $B^{0}_{\bar{R}\bar{L},RL}\left(\varepsilon\right)$ are the bare KKR structure constants as they are usually defined, albeit in real space. $C_{L\bar{L}l'} \equiv \int Y_L\left(\hat{\mathbf{r}}\right) Y^{*}_{\bar{L}}\left(\hat{\mathbf{r}}\right) Y_{l'(\bar{m}-m)}\left(\hat{\mathbf{r}}\right) d\hat{\mathbf{r}}$ are the Gaunt coefficients. We now define an on-site block as zero, $B^{0}_{R\bar{L},RL}\left(\varepsilon\right) \equiv 0$, and name $B^{0}\left(\varepsilon\right)$ the bare *structure matrix,* which is Hermitian. It is convenient to write the expansion (4) of the *bare* spherical waves, for any R' and $\bar{R}$ including $R'{=}\bar{R}$, symbolically as:

$$n^{0}\left(\varepsilon,\mathbf{r}\right) = j\left(\varepsilon,\mathbf{r}\right)\kappa^{-1}B^{0}\left(\varepsilon\right) + n\left(\varepsilon,\mathbf{r}\right) \tag{6}$$

where capitals denote matrices $\left(e.g.\ B^{0}\right)$, and lower case letters denote vectors $\left(e.g.\ j\left(\varepsilon,\mathbf{r}\right)\right)$ or diagonal matrices $\left(e.g.\ \kappa^{-1}\tan\alpha\left(\varepsilon\right)\right)$, specifically numbers $\left(e.g.\ \kappa\right)$. The spherical-harmonics expansions for the *screened* spherical wave, we write in the analogous way:

$$n^{\alpha}\left(\varepsilon,\mathbf{r}\right) = j^{\alpha}\left(\varepsilon,\mathbf{r}\right)\kappa^{-1}B^{\alpha}\left(\varepsilon\right) + n\left(\varepsilon,\mathbf{r}\right), \tag{7}$$

where $j^{\alpha}\left(\varepsilon,\mathbf{r}\right) \equiv j^{\alpha}_{RL}\left(\varepsilon,r\right) Y_L\left(\hat{\mathbf{r}}\right)$ and the radial function is that linear combination,

$$j^{\alpha}_{RL}\left(\varepsilon,r\right) \equiv j_l\left(\kappa r\right) - n_l\left(\kappa r\right)\tan\alpha_{RL}\left(\varepsilon\right), \tag{8}$$

which satisfies the partial boundary condition: For any active component this is that $j^{\alpha}_{RL}\left(\varepsilon,r\right)$ should vanish at the hard sphere so that we can substitute that radial component of $n^{\alpha}\left(\varepsilon,\mathbf{r}\right)$ continuously inside the hard sphere by zero. For any passive component this is that $j^{\alpha}_{RL}\left(\varepsilon,r\right)$ should match (have the same radial logarithmic derivative as) the radial Schrödinger solution, $\varphi_{Rl}\left(\varepsilon,r\right)$ given by (2), so that we can substitute that radial component of $n^{\alpha}\left(\varepsilon,\mathbf{r}\right)$ continuously and differentiably by $\varphi_{Rl}\left(\varepsilon,r\right)$. With these substitutions, $n^{\alpha}_{RL}\left(\varepsilon,\mathbf{r}\right)$ becomes the SSW, *i.e.,* we might write: $\psi^{\alpha}_{RL}\left(\varepsilon,\mathbf{r}\right) \equiv \tilde{n}^{\alpha}_{RL}\left(\varepsilon,\mathbf{r}\right)$ with the tilde denoting the substitutions. In conclusion, $\alpha_{RL}\left(\varepsilon\right)$ is the hard-sphere phase-shift for RL active $\left(A\right)$ and the real, potential-dependent phase-shift for RL passive $\left(P\right)$:

$$\alpha_{RL}\left(\varepsilon\right) = \begin{cases} \arctan\left\{j_l\left(\kappa a_R\right)/n_l\left(\kappa a_R\right)\right\} & \text{for} \quad RL \in A \\ \eta_{Rl}\left(\varepsilon\right) & \text{for} \quad RL \in P \end{cases}. \tag{9}$$

Due to the presence of the centrifugal potential in the radial Schrödinger equation (2), we have: $\lim_{l\to\infty}\eta_l\left(\varepsilon\right) = 0$, and this ensures that the L-dimension of the matrices dealt with in the multiple-scattering formalism is finite, *i.e.* $\max l \sim 3$. The passive partial waves with non-zero phase-shifts we call *intermediate* $\left(I\right)$.

The subscript RL, rather than Rl, on α and $j^{\alpha}\left(\varepsilon,r\right)$ takes into consideration that downfolding can be m-dependent, *e.g.* for the cuprates to be considered in the following section the conduction-band orbital is Cu $d_{x^2-y^2}$ with all other partial waves downfolded.

We finally need to express the *screening transformation,* $X^{\alpha}\left(\varepsilon\right)$, and the *screened structure matrix,* $B^{\alpha}\left(\varepsilon\right)$, in terms of the bare structure matrix given analytically by (5). We thus expand each term of the linear combination (3) in spherical-harmonics using (6), and compare with (7) using (8):

$$n^{\alpha}(\varepsilon,\mathbf{r})=\left\{\begin{array}{lcl} n^{0}(\varepsilon,\mathbf{r})\,X^{\alpha}(\varepsilon) & = & j(\varepsilon,\mathbf{r})\,\kappa^{-1}B^{0}(\varepsilon)\,X^{\alpha}(\varepsilon)\;+\;n(\varepsilon,\mathbf{r})\,X^{\alpha}(\varepsilon) \\ j^{\alpha}(\varepsilon,\mathbf{r})\,\kappa^{-1}B^{\alpha}(\varepsilon)+n(\varepsilon,\mathbf{r}) & = & j(\varepsilon,\mathbf{r})\,\kappa^{-1}B^{\alpha}(\varepsilon)+n(\varepsilon,\mathbf{r})\left[1-\kappa^{-1}\tan\alpha(\varepsilon)\,B^{\alpha}(\varepsilon)\right]\end{array}\right.$$

As a result:

$$X^{\alpha}(\varepsilon)\;=\;1-\kappa^{-1}\tan\alpha(\varepsilon)\,B^{\alpha}(\varepsilon)\,,\quad\text{where}\quad B^{\alpha}(\varepsilon)^{-1}\;=\;B^{0}(\varepsilon)^{-1}+\kappa^{-1}\tan\alpha(\varepsilon)\,,\tag{10}$$

or equivalently:

$$B^{\alpha}(\varepsilon)\;=\;\kappa\cot\alpha(\varepsilon)\;-\;\kappa\cot\alpha(\varepsilon)\left[\kappa\cot\alpha(\varepsilon)+B^{0}(\varepsilon)\right]^{-1}\kappa\cot\alpha(\varepsilon)\,.\tag{11}$$

Note that B^{α} in contrast to B^{0} has on-site elements. The screened structure matrix (11) completely specifies the set of SSWs. Whereas the bare structure matrix (5) is long ranged and strongly energy-dependent, the hard-sphere confinement makes the screened structure matrix localized in real space and weakly energy-dependent. We generate $B^{\alpha}_{RL,R'L'}(\varepsilon)$ by matrix inversion for clusters in real space (R), and the L-dimension limited by $\max l$.

In fact, for charge-selfconsistent NMTO calculations it is more efficient to compute, once for a given structure, a *strongly* screened structure matrix $B^{\beta}(\varepsilon)$ defined by having *hard-sphere* phase-shifts not only for the active, but also for the intermediate channels, that is:

$$\beta_{RL}(\varepsilon)=\arctan\left\{j_{l}(\kappa a_{R})\,/n_{l}(\kappa a_{R})\right\}\quad\text{for}\quad l\leq\max l,\quad \textit{i.e.},\ \text{for}\ RL\in A+I.\tag{12}$$

The strongly screened scattered waves are basically *cellular functions,* as may be seen from the front-page picture of Ref. [2]. In case we deal with a crystal with lattice translations $\mathbf{T}$, the strongly screened structure matrix is Block-summed to

$$B^{\beta}_{RL,R'L'}(\varepsilon,\mathbf{k})=\sum_{T}\exp(i\mathbf{k}\cdot\mathbf{T})\,B^{\beta}_{(\mathbf{R}+\mathbf{T})L,R'L'}(\varepsilon)\,.$$

Finally, the downfolded structure matrix $B^{\alpha}(\varepsilon)$, whose active block (A) will be used for solving Schrödinger's equation [see (19), (20), and (56)], is calculated in each iteration by partitioning:

$$B^{\alpha}_{AA}(\varepsilon)=B^{\beta}_{AA}(\varepsilon)-B^{\beta}_{AI}(\varepsilon)\left[\kappa\cot\eta_{I}(\varepsilon)+B^{\beta}_{II}(\varepsilon)\right]^{-1}B^{\beta}_{IA}(\varepsilon)\,.\tag{13}$$

It may be noted that although screening (3) is a linear transformation of the set of $n^{\alpha}(\varepsilon,\mathbf{r})$-functions, it is *not* a linear transformation of the set of $\psi^{\alpha}(\varepsilon,\mathbf{r})$-functions due to their augmentation. This was not the case in the 2nd-generation formalism. Downfolding is a special case of a screening transformation; it turns out to be a linear transformation followed by truncation of the inactive channels.

Kinked partial waves (KPWs) and the screened KKR equations

We now come to specify the KPW which has the SSW as its tail and first return to the Si sp-set illustrated in Fig. 2. We cut the p_{111}-KPW along the [111]-line from the central Si atom through its nearest neighbor and half-way into the back-bond void. The result is shown by the solid curve in Fig. 6 for an energy ε between ϵ_0 and ϵ_1. The kinks at the central and the nearest-neighbor a-spheres are clearly seen, and so is the downfolded d-character at the nearest neighbor. In fact, the KPW shown in Fig. 6 was not constructed from the Si_2E_2 potential used in Fig. 2, although it is indistinguishable from it on the scale of the figure, but from a potential $\sum_R v_R(r_R)$ where the spherically symmetric potential-wells $v_R(r)$ are centered exclusively on the atoms (no empty spheres) and have ranges s_R (=MT-radii) so large that the central MT-sphere in the present case reaches 3/4 the distance to the nearest-neighbor site. The overlap, defined as $\omega_{12} \equiv [(s_1+s_2)/|\mathbf{R}_1-\mathbf{R}_2|]-1$, is thus 50 per cent. In Fig. 6 the extent of the *central* MT-well is indicated by s. This kind of potential, where the MT-spheres can be as fat as van der Waals spheres, we call an *overlapping* MT-potential.

In order to construct the KPW in Fig. 6, we integrate the radial Schrödinger equation (2) numerically from the origin all the way to s, obtaining the partial wave $\varphi_l(\varepsilon,r)\,Y_L(\hat{\mathbf{r}})$ shown by the dot-dashed curve. From here, we continue the integration *smoothly backwards* from s to a over the *flat* potential $[v(r)\equiv 0]$, obtaining the phase-shifted partial wave $\varphi_l^o(\varepsilon,r)\,Y_L(\hat{\mathbf{r}})$ shown by the dotted curve. $\varphi_l(\varepsilon,r)$ and $\varphi_l^o(\varepsilon,r)$ match in value and slope at s, but their curvatures, which are given by the radial Schrödinger equation (2), differ because $v(r)$ goes discontinuously to zero at s, *i.e.,* $v(s)$ is finite. At the central a-sphere, $\varphi_l^o(\varepsilon,r)\,Y_L(\hat{\mathbf{r}})$ is joined *continuously* but with a kink to the SSW, $\psi^\alpha_{RL}(\varepsilon,\mathbf{r})$, shown by the dashed curve. In terms of these contributions, the KPW shown by the solid curve is

$$\phi^\alpha_{RL}(\varepsilon,\mathbf{r}) \;\equiv\; \left[\varphi^\alpha_{Rl}(\varepsilon,r_R)-\varphi^{o\,\alpha}_{Rl}(\varepsilon,r_R)\right]Y_L(\hat{\mathbf{r}}_R) \;+\; \psi^\alpha_{RL}(\varepsilon,\mathbf{r}), \tag{14}$$

where $\varphi(r)$ is truncated for $r>s$ and $\varphi^o(r)$ is truncated for $r<a$ and $r>s$. The first term goes quadratically to zero at the MT-sphere:

$$\varphi_l(\varepsilon,r)-\varphi_l^o(\varepsilon,r) \;=\; \frac{1}{2}(s-r)^2\,v(s)\,\varphi_l(\varepsilon,s) \;+\; o\left((s-r)^2\right), \tag{15}$$

and is therefore often called a *tongue.* The subscript α on φ and φ^o in (14) merely labels a normalization, which is such that the KPW is continuous. This implies that $\psi^\alpha_{RL}(\varepsilon,\mathbf{r})$ and $\varphi_l^o(\varepsilon,r)\,Y_L(\hat{\mathbf{r}})$ take the same value at the own sphere. The value of the former is $n_l(\kappa a_R)\,Y_L(\hat{\mathbf{r}}_R)$, according to (7) and the fact that $j^\alpha_{RL}(\varepsilon,a_R)\equiv 0$. As a consequence:

$$\varphi^{o\,\alpha}_{Rl}(\varepsilon,r)=\frac{n_l(\kappa a_R)}{j^\eta_{Rl}(\kappa a_R)}j^\eta_{Rl}(\kappa r)=\frac{j_l(\kappa r)-n_l(\kappa r)\tan\eta_{Rl}(\varepsilon)}{\tan\alpha_{RL}(\varepsilon)-\tan\eta_{Rl}(\varepsilon)}=n_l(\kappa r)-\cot\eta^\alpha_{RL}(\varepsilon)\,j^\alpha_{RL}(\varepsilon,r), \tag{16}$$

where we have used the definition (8) of j^η and j^α, and we have defined $\eta^\alpha(\varepsilon)$ as the phase shift with respect to the hard-sphere background:

$$\tan\eta^\alpha_{RL}(\varepsilon)\equiv\tan\eta_{Rl}(\varepsilon)-\tan\alpha_{RL}(\varepsilon). \tag{17}$$

We may finally use (7) to obtain the spherical-harmonics expansions of the KPW, valid at, and somewhat outside the hard spheres:

$$\begin{aligned}
\phi^\alpha(\varepsilon,\mathbf{r}) &= \varphi^\alpha(\varepsilon,\mathbf{r})-\varphi^{o\,\alpha}(\varepsilon,\mathbf{r})+j^\alpha(\varepsilon,\mathbf{r})\,\kappa^{-1}B^\alpha(\varepsilon)+n(\varepsilon,\mathbf{r}) \\
&= \varphi^\alpha(\varepsilon,\mathbf{r})+j^\alpha(\varepsilon,\mathbf{r})\,\kappa^{-1}\left[\kappa\cot\eta^\alpha(\varepsilon)+B^\alpha(\varepsilon)\right] \\
&\equiv \varphi^\alpha(\varepsilon,\mathbf{r})+j^\alpha(\varepsilon,\mathbf{r})\,\kappa^{-1}K^\alpha(\varepsilon).
\end{aligned} \tag{18}$$

Here, we have used (16) and have defined a *screened KKR matrix,* with the elements

$$K^{\alpha}_{RL,R'L'}(\varepsilon) \;=\; \kappa \cot \eta^{\alpha}_{RL}(\varepsilon)\, \delta_{RR'}\delta_{LL'} \;+\; B^{\alpha}_{RL,R'L'}(\varepsilon)\,. \tag{19}$$

This, or its inverse, the so-called *scattering-path operator* $K^{\alpha}(\varepsilon)^{-1} \equiv G^{\alpha}(\varepsilon)$, is the central quantity of multiple-scattering and MTO theory. Comparison of (19) with (11) shows that, apart from additive and multiplicative normalizations, the screened structure matrix is the scattering-path operator for the repulsive potential specified by the phase-shifts (9).

From the expansions (18), it is intuitively clear, and the details will be discussed below in connection with Eq. (24), that any linear combination $\sum_{RL\in A}\phi^{\alpha}_{RL}(\varepsilon_i,\mathbf{r})\,c^{\alpha}_{RL,i}$ of KPWs, with the property that

$$\sum_{RL\in A} K^{\alpha}_{R'L',RL}(\varepsilon_i)\; c^{\alpha}_{RL,i} \;=\; 0, \quad \text{for all active } R'L', \tag{20}$$

is a solution $\Psi_i(\mathbf{r})$ with energy ε_i of Schrödinger's equation because the eigenvector $c^{\alpha}_{RL,i}$ leaves behind the partial-wave expansions $\sum_{RL}\varphi^{\alpha}_{RL}(\varepsilon_i,\mathbf{r})\,c^{\alpha}_{RL,i}$, which are solutions by construction. The linear, homogeneous equations (20) are the *screened KKR equations*, and the energy ε_i is determined by the condition that these equations have a proper solution, *i.e.* that $\det K^{\alpha}(\varepsilon_i) = 0$.

In order to get rid of the spurious $\sqrt{\varepsilon}$-dependences and to obtain a Hamiltonian formalism [see Eq. (29)], it is convenient to *renormalize* the SSW to have value $Y_L(\hat{\mathbf{r}})$ at its own hard sphere and, hence, to renormalize $\varphi^{o\alpha}_{Rl}(\varepsilon, r_R)$ to be unity for $r_R = a_R$, and to renormalize the partial wave and the KPW accordingly. Denoting these renormalized functions by the superscript a, which refers to hard-sphere radii rather than to hard-sphere phase-shifts α, we thus have:

$$\psi^{a}_{RL}(\varepsilon,\mathbf{r}) \equiv \frac{\psi^{\alpha}_{RL}(\varepsilon,\mathbf{r})}{n_l(\kappa a_{RL})}, \qquad \varphi^{o\,a}_{Rl}(\varepsilon, a_{RL}) \equiv 1, \quad \text{and} \quad \phi^{a}_{RL}(\varepsilon,\mathbf{r}) \equiv \frac{\phi^{\alpha}_{RL}(\varepsilon,\mathbf{r})}{n_l(\kappa a_{RL})}. \tag{21}$$

These are the normalizations used in all figures. The KKR matrix is renormalized to what we call the *kink matrix:*

$$K^{a}_{RL,R'L'}(\varepsilon) \;\equiv\; \frac{-K^{\alpha}_{RL,R'L'}(\varepsilon)}{\kappa n_l(\kappa a_R)\;\kappa n_{l'}(\kappa a_{R'})}, \tag{22}$$

which obviously remains Hermitian. The expansion (18), the Wronskian relation $j^{\alpha}(\varepsilon,a)' = -1/a^2\kappa n(\kappa a)$ with $' \equiv \partial/\partial r$, and the renormalizations (21) and (22) show that $K^{a}_{RL,R'L'}(\varepsilon)$ is the kink of $\phi_{R'L'}(\varepsilon,\mathbf{r})$ at the a_R-sphere, projected onto $Y_L(\hat{r}_R)/a_R^2$. The inverse of the kink matrix we call the *Green matrix:*

$$G^{a}(\varepsilon) \equiv K^{a}(\varepsilon)^{-1}\,. \tag{23}$$

In the following we shall always use this a-normalization, and since from now on we shall seldom change the screening, we usually drop the superscript a.

Due to its kinks, an individual KPW is not a solution of Schrödinger's equation, but any *smooth* linear combination of KPWs *is.* For coefficients $c_{RL,i}$ such that the kink in Fig. 6 between $\varphi^{o}_{R'l'}(\varepsilon_i, r_{R'})\,Y_{L'}(\hat{\mathbf{r}}_{R'})$ and $\psi_{R'L'}(\varepsilon_i,\mathbf{r})$ on the central sphere (R') is cancelled by the sum of the kinks from the tails of the KPWs on the neighbors, that is, for a solution of the kink-cancellation equations (20) (using a-normalization), we have:

$$\varphi^{o}_{R'l'}(\varepsilon_i, r_{R'})\, c_{R'L',i} = \mathcal{P}_{R'L'} \sum_{RL\in A} \psi_{RL}(\varepsilon_i,\mathbf{r})\, c_{RL,i}, \tag{24}$$

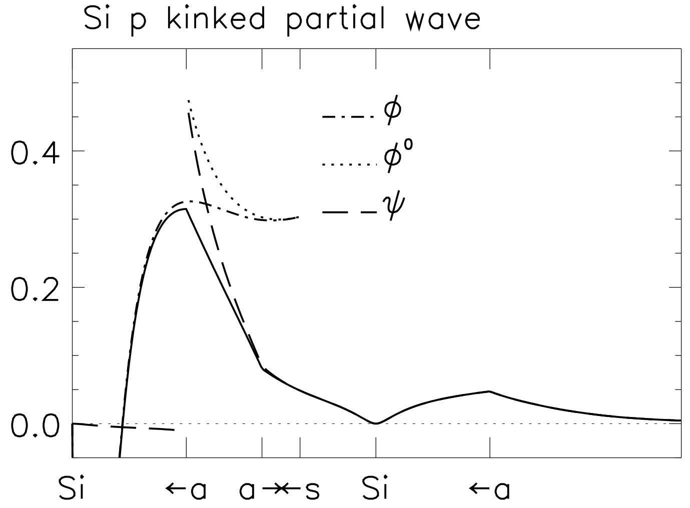

Figure 6: Si p_{111}-KPW for the Si *sp*-set and its constituents φY, $\varphi^o Y$, and ψ. The MT-potential used no empty spheres. s denotes the range of the central well. The a's indicate the hard spheres at the central and the nearest-neighbor sites.

where $\mathcal{P}_{R'L'}$ projects onto an active $Y_{L'}\left(\hat{r}_{R'}\right)$. This equation holds because both the left and the right-hand sides are solutions of the radial wave equation with the same value and slope at $a_{R'}$ and, hence, they are identical. With (24) satisfied, the KPW-definition (14) yields

$$\begin{aligned}\sum_{RL\in A}\phi_{RL}\left(\varepsilon_i,\mathbf{r}\right)c_{RL,i} &= \sum_{l'=0}^{\infty}\sum_{m'=-l}^{l}\varphi_{R'l'}\left(\varepsilon_i,r_{R'}\right)Y_{L'}\left(\hat{\mathbf{r}}_{R'}\right)c_{R'L',i} \\ &\quad+\sum_{R(\neq R')L\in A}\left[\varphi_{Rl}\left(\varepsilon_i,r_R\right)-\varphi_{Rl}^{o}\left(\varepsilon_i,r_R\right)\right]Y_L\left(\hat{\mathbf{r}}_R\right)c_{RL,i},\end{aligned} \tag{25}$$

for $\mathbf{r}$ inside a sphere, centered at $\mathbf{R}'$ and passing through the center of the nearest neighbor. In (25) the first term is a solution of Schrödinger's equation by construction and the l'-sum is infinite because the partial-wave expansions of the SSWs at the neighboring sites include passive as well as active partial waves. In the second term, $\varphi-\varphi^o$ vanishes outside its own MT-sphere, and this second term therefore vanishes outside all MT-spheres different from the central one. If the MT-spheres do not overlap, (25) therefore solves Schrödinger's equation exactly. If the potential-well from a neighboring site (R) *overlaps* the central site (R'), then the $\varphi_{RL}-\varphi_{RL}^{\circ}$ tongues (15) stick into the MT-sphere at R' and cause an error. To find its size, we operate with the Hamiltonian for the overlapping MT-potential,

$$\mathcal{H}\ \equiv\ -\nabla^2\ +\ \sum_{R'}v_{R'}\left(r_{R'}\right)\ , \tag{26}$$

on the smooth function

$$\Psi_i\left(\mathbf{r}\right)\ \equiv\ \sum_{RL\in A}\phi_{RL}\left(\varepsilon_i,\mathbf{r}_R\right)c_{RL,i}, \tag{27}$$

of which (25) is the expansion around site R', and obtain:

$$\begin{aligned}\left(\mathcal{H}-\varepsilon_i\right)\Psi_i\left(\mathbf{r}\right) &= \sum_{R'}v_{R'}\left(r_{R'}\right)\sum_{R(\neq R')L\in A}\left[\varphi_{Rl}\left(\varepsilon_i,r_R\right)-\varphi_{Rl}^{\circ}\left(\varepsilon_i,r_R\right)\right]Y_L\left(\hat{\mathbf{r}}_R\right)c_{RL,i} \\ &\sim \frac{1}{2}\sum_{RR'}^{pairs}v_{R'}\left(s_{R'}\right)\left[\left(s_{R'}-r_{R'}\right)^2+\left(s_R-r_R\right)^2\right]v_R\left(s_R\right)\Psi_i\left(\mathbf{r}\right).\end{aligned} \tag{28}$$

This shows that the smooth linear combination (27) of KPWs, given by the solution of the KKR equations (20), solves Schrödinger's equation for the *superposition* of MT-wells to within an error which is of *second order in the potential overlap* [13, 3]. If needed, the kinetic-energy error (28) can be corrected for, and the simplest correction is to use merely:

$$\Delta\varepsilon_i \approx \langle \Psi_i | \mathcal{H} - \varepsilon_i | \Psi_i \rangle \sim \frac{1}{2} \sum_{RR' \in pairs} v_{R'}\left(s_{R'}\right) \left[\left(s_{R'} - r_{R'}\right)^2 + \left(s_R - r_R\right)^2 \right] v_R\left(s_R\right) \rho_{R'R,i}\,,$$

to correct the KKR energy ε_i. Here, $\rho_{R'R,i}$ is the probability that state i is inside the overlap of the MT-spheres at sites R and R'.

Since the kink matrix (22) specifies the kinks of the KPW-set, it also specifies how the MT-Hamiltonian operates on the set of kinked partial waves, specifically:

$$(\mathcal{H} - \varepsilon)\, \phi_{R'L'}(\varepsilon, \mathbf{r}) = -\sum_{RL \in A} \delta\left(r_R - a_R\right) Y_L\left(\hat{\mathbf{r}}_R\right) K_{RL,R'L'}(\varepsilon)\,. \tag{29}$$

The overlap-integral between two KPWs may be obtained by use of Green's second theorem and the result is simply:

$$\begin{aligned} \left\langle \phi_{R'L'}\left(\varepsilon'\right) \mid \phi_{RL}(\varepsilon) \right\rangle \;&=\; \left\langle \psi_{R'L'}\left(\varepsilon'\right) \mid \psi_{RL}(\varepsilon) \right\rangle \;+ \\ &\delta_{R'R}\delta_{L'L} \left(\int_0^{s_R} \varphi_{RL}\left(\varepsilon', r\right) \varphi_{RL}(\varepsilon, r)\, r^2 dr - \int_{a_R}^{s_R} \varphi^{\circ}_{RL}\left(\varepsilon', r\right) \varphi^{\circ}_{RL}(\varepsilon, r)\, r^2 dr \right) \\ = \quad \frac{K_{R'L',RL}\left(\varepsilon'\right) - K_{R'L',RL}(\varepsilon)}{\varepsilon' - \varepsilon} &\quad \longrightarrow \dot{K}_{R'L',RL}(\varepsilon) \quad \text{if} \quad \varepsilon' \to \varepsilon. \end{aligned} \tag{30}$$

Here, $\dot{} \equiv \partial/\partial\varepsilon$ and the diagonal part of the integral has been calculated the '3-fold way' indicated in Fig. 6. This means that all cross-terms between products of ψ, φ, and φ°-functions, and between φ or φ°-functions on different sites are neglected. For solutions of the KKR equations, this gives the correct result due to the cancellation discussed in connection with expression (24). The KKR eigen(column)vector c_i should be normalized according to: $1 = c_i^{\dagger} \dot{K}\left(\varepsilon_i\right) c_i$ in order that $\langle \Psi_i \mid \Psi_i \rangle = 1$.

An accurate approximation for the *charge density,* which is consistent with the 3-fold way and, hence, with the normalization has the following *simple* form:

$$\rho(\mathbf{r}) \equiv \sum_{RR'} \sum_{LL'} \int^{\varepsilon_F} \phi_{RL}\left(\varepsilon, \mathbf{r}_R\right)\, N_{RL,R'L'}(\varepsilon)\, \phi_{R'L'}\left(\varepsilon, \mathbf{r}_{R'}\right)^* d\varepsilon = \rho^{\psi}(\mathbf{r}) + \sum_R \left[\rho^{\varphi}_R\left(\mathbf{r}_R\right) - \rho^{\varphi^{\circ}}_R\left(\mathbf{r}_R\right) \right] \tag{31}$$

where the global contribution is:

$$\rho^{\psi}(\mathbf{r}) \equiv \sum_{RR'} \sum_{LL'} \int^{\varepsilon_F} \psi_{RL}\left(\varepsilon, \mathbf{r}_R\right)\, N_{RL,R'L'}(\varepsilon)\, \psi_{R'L'}\left(\varepsilon, \mathbf{r}_{R'}\right)^* d\varepsilon \tag{32}$$

and the local contributions, $\rho^{\varphi}_R\left(\mathbf{r}_R\right) - \rho^{\varphi^{\circ}}_R\left(\mathbf{r}_R\right)$, which vanish quadratically at their respective MT-sphere, are:

$$\begin{aligned} \rho^{\varphi}_R(\mathbf{r}) \;&=\; \sum_{LL'} Y_L(\hat{\mathbf{r}})\, Y^*_{L'}(\hat{\mathbf{r}}) \int^{\varepsilon_F} \varphi_{Rl}(\varepsilon, r)\, N_{RL,RL'}(\varepsilon)\, \varphi_{Rl'}(\varepsilon, r)\, d\varepsilon \\ \rho^{\varphi^{\circ}}_R(\mathbf{r}) \;&=\; \sum_{LL'} Y_L(\hat{\mathbf{r}})\, Y^*_{L'}(\hat{\mathbf{r}}) \int^{\varepsilon_F} \varphi^{\circ}_{Rl}(\varepsilon, r)\, N_{RL,RL'}(\varepsilon)\, \varphi^{\circ}_{Rl'}(\varepsilon, r)\, d\varepsilon\,. \end{aligned} \tag{33}$$

The common density-of-states matrix in these equations is:

$$N_{RL,R'L'}(\varepsilon)=\sum_{i\in occ}c_{RL,i}\delta(\varepsilon-\varepsilon_i)\,c^*_{R'L',i}=\frac{1}{\pi}\mathrm{Im}G_{RL,R'L'}(\varepsilon+i\delta). \tag{34}$$

We will evaluate the charge density locally, that is: pick a site R and find $\rho(\mathbf{r})$ in its neighborhood. For that purpose, we 'blow up' from the downfolded a-representation specified by (9) to the strongly screened b-representation specified by (12). We thus need

$$G^b_{AA}(\varepsilon)=K^a_{AA}(\varepsilon)^{-1}=G^a_{AA}(\varepsilon)\equiv G^a(\varepsilon)\quad\text{and}\quad G^b_{IA}(\varepsilon)=-K^b_{II}(\varepsilon)^{-1}K^b_{IA}(\varepsilon)\,G^b_{AA}(\varepsilon). \tag{35}$$

The P-part of $G^a(\varepsilon)$ vanishes because the P-part of $K^a(\varepsilon)$ is diagonal with diverging elements. Note that the product $K^b_{II}(\varepsilon)^{-1}K^b_{IA}(\varepsilon)$ was used already for the downfolding (13).

Muffin-tin orbitals (MTOs) and their Hamiltonian and overlap matrices

Since computation of the kink-matrix is expensive, it is not efficient to find a one-electron energy from: $\det K(\varepsilon_i)=0$, and then solve the linear equations for the corresponding $c_{RL,i}$. Rather, we shall construct an energy- and state-independent basis set of Nth-order MTOs, so-called NMTOs (1), with the property that it spans any wave function $\Psi_i(\mathbf{r})$ with energy ε_i in the neighborhood of $N{+}1$ chosen energies, $\epsilon_0,...,\epsilon_N$, to within an error proportional to $(\varepsilon_i-\epsilon_0)...(\varepsilon_i-\epsilon_N)$. Solution of the generalized eigenvalue problem,

$$\sum_{RL\in A}\left\langle\chi^{(N)}_{R'L'}\left|\mathcal{H}-\varepsilon_i\right|\chi^{(N)}_{RL}\right\rangle b_{RL,i}\;=\;0,\quad\text{for all active }R'L', \tag{36}$$

then yields energies with errors proportional to $(\varepsilon_i-\epsilon_0)^2...(\varepsilon_i-\epsilon_N)^2$ by virtue of the variational principle. This procedure has the added bonus that perturbations to the overlapping MT-Hamiltonian $\mathcal{H}$ are easily included.

It can be proved [5] that the error of the wave functions introduced by using the 3-fold way is proportional to $(r_R-a_R)^{2N+1}(\varepsilon_i-\epsilon_0)...(\varepsilon_i-\epsilon_N)$. The 3-fold way is therefore a consistent approximation, not only in the KKR, but also in the NMTO method.

MTOs with $N=0$

We have seen that all wave functions with $\varepsilon_i=\epsilon_0$ may be expressed as $\sum_{RL}\phi_{RL}(\epsilon_0,\mathbf{r})\,c_{RL,i}$. Therefore, the MTOs with $N=0$ are simply the KPWs at the chosen energy: $\chi^{(0)}_{RL}(\mathbf{r})=\phi_{RL}(\epsilon_0,\mathbf{r})$. In the basis of these, the Hamiltonian and overlap matrices are given by respectively:

$$\left\langle\chi^{(0)}\left|\mathcal{H}-\epsilon_0\right|\chi^{(0)}\right\rangle=-K(\epsilon_0)\quad\text{and}\quad\left\langle\chi^{(0)}\mid\chi^{(0)}\right\rangle=\dot{K}(\epsilon_0), \tag{37}$$

as may easily be found from Eq. (29) and the normalization chosen. Since neglect of the off-diagonal elements of the overlap matrix, normalized to have diagonal elements 1, only causes errors in the energy bands of second order,

$$\tilde{K}_{RL,R'L'}(\epsilon_0)\;\equiv\;-\dot{K}_{RL,RL}(\epsilon_0)^{-\frac{1}{2}}\,K_{RL,R'L'}(\epsilon_0)\,\dot{K}_{R'L',R'L'}(\epsilon_0)^{-\frac{1}{2}} \tag{38}$$

is a *first-order, two-centre, tight-binding Hamiltonian.*

MTOs with $N > 0$

By an equation of the usual type:

$$\left(\mathcal{H}-\varepsilon\right)\gamma_{RL}\left(\varepsilon,\mathbf{r}\right)=-\delta\left(r_R-a_R\right)Y_L\left(\hat{\mathbf{r}}_R\right), \tag{39}$$

we define a *contracted Green function,* $\gamma_{RL}\left(\varepsilon,\mathbf{r}\right)$, which has one of its spatial variables confined to the a-spheres, *i.e.* $\mathbf{r}'\to RL$. Considered a function of $\mathbf{r}$, this contracted Green function is a (possibly delocalized, impurity-) solution with energy ε of Schrödinger's equation, except at its own sphere and for its own angular momentum where it has a kink of size unity. This kink becomes negligible when ε is close to a one-electron energy because the Green function has a pole there. Comparison of Eq. (39) with Eq. (29) now shows that

$$\gamma\left(\varepsilon,\mathbf{r}\right)=\phi\left(\varepsilon,\mathbf{r}\right)G\left(\varepsilon\right). \tag{40}$$

The contracted Green function is thus factorized into a matrix, $G\left(\varepsilon\right)$, which has the full energy dependence, and a vector of functions, $\phi\left(\varepsilon,\mathbf{r}\right)$, which has the full spatial dependence and a weak energy dependence [14]. We now want to factorize the $\mathbf{r}$ and ε-dependences completely and, hence, to approximate $\phi\left(\varepsilon,\mathbf{r}\right)G\left(\varepsilon\right)$ by $\chi^{(N)}\left(\mathbf{r}\right)G\left(\varepsilon\right)$:

We note that subtracting from the contracted Green function a function $\omega^{(N)}\left(\varepsilon,\mathbf{r}\right)$ which is analytical in energy,

$$\phi\left(\varepsilon,\mathbf{r}\right)G\left(\varepsilon\right)\;-\;\omega^{(N)}\left(\varepsilon,\mathbf{r}\right)\;\equiv\;\chi^{(N)}\left(\varepsilon,\mathbf{r}\right)G\left(\varepsilon\right), \tag{41}$$

produces an equally good Green function, in the sense that both yield the same Schrödinger-equation solutions. If we can therefore determine the vector $\omega^{(N)}\left(\varepsilon,\mathbf{r}\right)$ of analytical functions in such a way that each $\chi_{RL}^{(N)}\left(\varepsilon,\mathbf{r}\right)$ takes the *same* value, $\chi_{RL}^{(N)}\left(\mathbf{r}\right)$, at *all* energies, $\epsilon_0,...,\epsilon_N$, then

$$\chi_{RL}^{(N)}\left(\varepsilon,\mathbf{r}\right)\;=\;\chi_{RL}^{(N)}\left(\mathbf{r}\right)\;+\;O\left(\left(\varepsilon-\epsilon_0\right)...\left(\varepsilon-\epsilon_N\right)\right),$$

and hence, $\chi^{(N)}\left(\mathbf{r}\right)$ is the set of NMTOs!

At this stage we need to remember that the divided differences of a function $f\left(\varepsilon\right)$ on an energy mesh are given by a table of the form:

$$\begin{array}{llll}
\epsilon_0 & f\left(\epsilon_0\right)\equiv f_0 & & \\
 & & \frac{f_0-f_1}{\epsilon_0-\epsilon_1}\equiv\frac{\Delta f}{\Delta[01]} & \\
\epsilon_1 & f\left(\epsilon_1\right)\equiv f_1 & & \frac{\frac{\Delta f}{\Delta[01]}-\frac{\Delta f}{\Delta[12]}}{\epsilon_0-\epsilon_2}\equiv\frac{\Delta^2 f}{\Delta[012]}\;, \\
 & & \frac{f_1-f_2}{\epsilon_1-\epsilon_2}\equiv\frac{\Delta f}{\Delta[12]} & \\
\epsilon_2 & f\left(\epsilon_2\right)\equiv f_2 & &
\end{array}$$

and that if the mesh condenses onto the energy ϵ_ν,

$$\frac{\Delta^N f}{\Delta\left[0...N\right]}\quad\to\quad\frac{1}{N!}\overset{(N)}{f}\left(\epsilon_\nu\right). \tag{42}$$

Now, since

$$\chi^{(N)}\left(\epsilon_0,\mathbf{r}\right)\;=\;\chi^{(N)}\left(\epsilon_1,\mathbf{r}\right)\;=\;...\;=\;\chi^{(N)}\left(\epsilon_N,\mathbf{r}\right),$$

the Nth divided difference of $\chi^{(N)}(\varepsilon,\mathbf{r})\,G(\varepsilon)$ equals $\chi^{(N)}(\mathbf{r})$ times the Nth divided difference of $G(\varepsilon)$. Moreover, if we let $\omega^{(N)}(\varepsilon,\mathbf{r})$ be a polynomial in energy of (N-1)st degree, its Nth divided difference on the mesh will vanish. Taking the Nth divided difference of (41), therefore leads to the following solution for the NMTO set:

$$\chi^{(N)}(\mathbf{r})\,\frac{\Delta^N G}{\Delta[0...N]} = \frac{\Delta^N \gamma(\mathbf{r})}{\Delta[0...N]} = \frac{\Delta^N \phi(\mathbf{r})\,G}{\Delta[0...N]}. \tag{43}$$

In order to obtain the explicit expression for the matrix weights in (1), we need to take the Nth divided difference of the product $\phi(\varepsilon,\mathbf{r})\,G(\varepsilon)$. For this purpose we recall the *Lagrange* expression

$$f^{(N)}(\varepsilon) = \sum_{n=0}^{N} f(\epsilon_n)\, l_n^{(N)}(\varepsilon), \quad \text{with} \quad l_n^{(N)}(\varepsilon) \equiv \prod_{m=0,\neq n}^{N} \frac{\varepsilon-\epsilon_m}{\epsilon_n-\epsilon_m}, \tag{44}$$

for the Nth degree polynomial $f^{(N)}(\varepsilon)$ which passes through the $N+1$ mesh points. Differentiating this polynomial N times yields the desired expression for the Nth divided difference:

$$\frac{\Delta^N f}{\Delta[0...N]} = \frac{1}{N!}\frac{d^N f^{(N)}(\varepsilon)}{d\varepsilon^N} = \sum_{n=0}^{N} f(\epsilon_n)\,\frac{d^N l_n^{(N)}(\varepsilon)}{d\varepsilon^N} = \sum_{n=0}^{N} \frac{f(\epsilon_n)}{\prod_{m=0,\neq n}^{N}(\epsilon_n-\epsilon_m)}. \tag{45}$$

This shows, by the way, that the Nth divided difference depends on the $N+1$ energies to which it refers, but not on their order. By use of (45) we obtain the desired expression:

$$L_n^{(N)} = \frac{G(\epsilon_n)}{\prod_{m=0,\neq n}^{N}(\epsilon_n-\epsilon_m)}\left[\frac{\Delta^N G}{\Delta[0...N]}\right]^{-1}, \tag{46}$$

in terms of the values of the Green matrix on the energy mesh. From (46) we immediately see that $\sum_{n=0}^{N} L_n^{(N)} = 1$, which ensures that $\chi_{RL}^{(N)}(\mathbf{r}) \sim \phi_{RL}(\varepsilon,\mathbf{r})$ in case the KPW-set varies little over the mesh. We also realize that the NMTO-set (1) may be interpreted as Lagrange interpolation of the energy-dependence of the KPW-set, with the weights being energy-independent matrices, $L_n^{(N)}$, rather than Nth-degree scalar polynomials, $l_n^{(N)}(\varepsilon)$. Finally, we emphasize that the size of the NMTO basis is independent of N, but as N increases each basis function may become more and more complicated.

We now work out the effect of the Hamiltonian on the NMTO set. It follows from (43) that NMTOs with $N>0$ are smooth, because the kinks of the functions $\gamma(\varepsilon,\mathbf{r})$ are equal to unity and thereby independent of energy. Since the NMTOs with $N>0$ are smooth, the contributions from the delta-function on the right-hand side of (39) for the contracted Green function will cancel in the end, and the effect of operating on (41) is therefore effectively:

$$\mathcal{H}\chi^{(N)}(\varepsilon,\mathbf{r})\,G(\varepsilon) = \mathcal{H}\gamma(\varepsilon,\mathbf{r}) - \mathcal{H}\omega^{(N)}(\varepsilon,\mathbf{r}) = \varepsilon\gamma(\varepsilon,\mathbf{r}) - \mathcal{H}\omega^{(N)}(\varepsilon,\mathbf{r}).$$

Taking again the Nth divided differences for the mesh on which $\chi^{(N)}(\varepsilon,\mathbf{r})$ is constant, yields:

$$\mathcal{H}\chi^{(N)}(\mathbf{r})\,\frac{\Delta^N G}{\Delta[0...N]} = \mathcal{H}\frac{\Delta^N \gamma(\mathbf{r})}{\Delta[0...N]} = \frac{\Delta^N \varepsilon\gamma(\mathbf{r})}{\Delta[0...N]}. \tag{47}$$

Before we continue with the evaluation of the NMTO Hamiltonian and overlap matrices to be used in the generalized eigenvalue problem (36), we derive a few illuminating relations:

Using again Eq. (45) and picking for instance the last mesh point, we obtain:

$$\begin{aligned}\frac{\Delta^N(\varepsilon-\epsilon_N)f}{\Delta[0...N]} &= \sum_{n=0}^{N}\frac{(\epsilon_n-\epsilon_N)f(\epsilon_n)}{\prod_{m=0,\neq n}^{N}(\epsilon_n-\epsilon_m)}=\sum_{n=0}^{N-1}\frac{(\epsilon_n-\epsilon_N)f(\epsilon_n)}{\prod_{m=0,\neq n}^{N}(\epsilon_n-\epsilon_m)}=\sum_{n=0}^{N-1}\frac{f(\epsilon_n)}{\prod_{m=0,\neq n}^{N-1}(\epsilon_n-\epsilon_m)}\\ &= \frac{\Delta^{N-1}f}{\Delta[0..N-1]}.\end{aligned}$$

As a consequence:

$$(\mathcal{H}-\epsilon_N)\chi^{(N)}(\mathbf{r})\frac{\Delta^N G}{\Delta[0...N]} = (\mathcal{H}-\epsilon_N)\frac{\Delta^N\gamma(\mathbf{r})}{\Delta[0...N]} = \frac{\Delta^{N-1}\gamma(\mathbf{r})}{\Delta[0..N-1]}. \tag{48}$$

Solving for the NMTOs (43) yields:

$$(\mathcal{H}-\epsilon_N)\chi^{(N)}(\mathbf{r}) = \chi^{(N-1)}(\mathbf{r})\left(E^{(N)}-\epsilon_N\right), \tag{49}$$

where $\chi^{(N-1)}(\mathbf{r})$ is the energy-independent MTO of order $N-1$, obtained by *not* using the *last* point, and where

$$E^{(N)} \equiv \epsilon_N+\frac{\Delta^{N-1}G}{\Delta[0..N-1]}\left[\frac{\Delta^N G}{\Delta[0...N]}\right]^{-1} = \frac{\Delta^N\varepsilon G}{\Delta[0...N]}\left[\frac{\Delta^N G}{\Delta[0...N]}\right]^{-1} = \sum_{n=0}^{N}\epsilon_n L_n^{(N)}, \tag{50}$$

is the *energy matrix* which, in contrast to $\chi^{(N-1)}(\mathbf{r})$ is independent of which mesh point is omitted. The first equation (50) shows how to compute $E^{(N)}$ and the last equation shows that $E^{(N)}$ is the energy *weighted* on the $0...N$-mesh by the Lagrange matrices (46).

Let us next consider a sequence of energy meshes, starting with the single-point mesh ϵ_0, then adding ϵ_1 in order to obtain the two-point mesh ϵ_0, ϵ_1, then adding ϵ_2 obtaining the three-point mesh ϵ_0, ϵ_1, ϵ_2, a.s.o. Associated with these meshes we obtain a sequence of NMTO sets: the KPW-set $\chi^{(0)}(\mathbf{r})$, the LMTO-set $\chi^{(1)}(\mathbf{r})$, the QMTO-set $\chi^{(2)}(\mathbf{r})$, a.s.o. Working *downwards*, we thus always *delete* the point with the *highest* index. Equation (49) now shows that with respect to the *order* of the NMTO-set, $\mathcal{H}-\epsilon_N$ may be viewed as a *step-down* operator and $E^{(N)}-\epsilon_N$ as the corresponding *transfer matrix.* In this sequence we may include the case $N{=}0$ provided that we define: $E^{(0)}-\epsilon_0\equiv -K(\epsilon_0)$ and $\chi^{(-1)}(\mathbf{r})\equiv\delta(\mathbf{r})$. Hence, $N+1$ successive step-down operations on the NMTO-set yield:

$$(\mathcal{H}-\epsilon_0)...(\mathcal{H}-\epsilon_N)\,\chi^{(N)}(\mathbf{r}) = \delta(\mathbf{r})\left(E^{(0)}-\epsilon_0\right)...\left(E^{(N)}-\epsilon_N\right).$$

This, first of all tells us that one has to operate N times with ∇^2, that is with ∇^{2N}, before getting to the non-smoothness of an NMTO, and secondly, that the higher the N, the more spread out the NMTO.

By taking matrix elements of (49), the transfer matrix may be expressed as:

$$E^{(N)}-\epsilon_N = \left\langle\chi^{(N)}\mid\chi^{(N-1)}\right\rangle^{-1}\left\langle\chi^{(N)}\left|\mathcal{H}-\epsilon_N\right|\chi^{(N)}\right\rangle. \tag{51}$$

This holds also for $N{=}0$, provided that we take the value of $\chi^{(0)}(\mathbf{r})$ at its screening sphere to be $\varphi^{\circ a}(\varepsilon,a)=1$ [as is also dictated by the 3-fold way (30)] so that $\left\langle\chi^{(0)}\mid\chi^{(-1)}\right\rangle=1$. The form (51) shows that the transfer matrices with $N\geq 1$ are *not* Hermitian but short ranged, as one may realize by recursion starting from $N{=}0$. Finally, it should be remembered that the NMTOs considered sofar have particular normalizations (which are *not:* $\left\langle \chi^{(N)} \mid \chi^{(N)} \right\rangle = 1$), and so do the transfer matrices.

Instead of using the Lagrange form (45) to factorize the NMTO (43), one may use the step-down property (49) to obtain:

$$\chi^{(N)}(\mathbf{r}) \;=\; \phi(\epsilon_N, \mathbf{r}) + \frac{\Delta\phi(\mathbf{r})}{\Delta[N-1,N]}\left(E^{(N)} - \epsilon_N\right) + ... + \frac{\Delta^N\phi(\mathbf{r})}{\Delta[0...N]}\left(E^{(1)} - \epsilon_1\right)..\left(E^{(N)} - \epsilon_N\right), \tag{52}$$

since from (29) and (48)

$$(\mathcal{H} - \epsilon_N)\,\phi(\epsilon_N, \mathbf{r}) = -\delta_{N,0}\,\delta(\mathbf{r})\,K(\epsilon_0) \quad \text{and} \quad (\mathcal{H} - \epsilon_N)\,\frac{\Delta^{N-M}\phi(\mathbf{r})}{\Delta[M...N]} = \frac{\Delta^{N-M-1}\phi(\mathbf{r})}{\Delta[M..N-1]}.$$

Expression (52) for the NMTO-set is the matrix equivalent -or the quantized form- of *Newton's* expression,

$$f^{(N)}(\varepsilon) \;=\; f(\epsilon_N) + \frac{\Delta f}{\Delta[N-1,N]}(\varepsilon - \epsilon_N) + ... + \frac{\Delta^N f}{\Delta[0...N]}(\varepsilon - \epsilon_1)..(\varepsilon - \epsilon_N), \tag{53}$$

for the Nth-degree polynomial (44) passing through the $N+1$ mesh points. In this case, $f(\epsilon_n) = \phi_{RL}(\epsilon_n, \mathbf{r})$. The Newton form (52) expresses the NMTO as a kinked partial wave at the same site and with the same angular momentum, plus a smoothing cloud of energy-derivative functions centered at all sites and with all angular momenta. This is clearly illustrated in Figs. 1-3. For a condensed mesh and using (42), the Newton expression (52) for the NMTO-set obviously reduces to the matrix-equivalent of the *Taylor* series for the energy-dependence of $\phi_{RL}(\varepsilon, \mathbf{r})$.

To calculate the NMTO *Hamiltonian* and *overlap matrices* we use expression (43) for the NMTO-set and therefore first need to evaluate the Hamiltonian and overlap matrices for the Nth divided difference of the contracted Green function (40). Since according to (48), operation with the Hamiltonian on this Nth divided difference yields the (N-1)st divided difference, we need expressions for $\left\langle \Delta^N\gamma/\Delta[0...N] \mid \Delta^N\gamma/\Delta[0...N] \right\rangle$ and $\left\langle \Delta^N\gamma/\Delta[0...N] \mid \Delta^{N-1}\gamma/\Delta[0..N-1] \right\rangle$. Pre and post-multiplication of the KPW overlap matrix (30) with the appropriate Green matrices yield

$$\langle \gamma(\varepsilon') \mid \gamma(\varepsilon) \rangle \;=\; -\frac{G(\varepsilon') - G(\varepsilon)}{\varepsilon' - \varepsilon} \quad \longrightarrow \; -\dot{G}(\varepsilon) \;=\; G(\varepsilon)\,\dot{K}(\varepsilon)\,G(\varepsilon) \quad \text{if } \varepsilon' \to \varepsilon,$$

and taking then the Nth divided difference with respect to ε' and the Mth divided difference with respect to ε gives:

$$\left\langle \frac{\Delta^N\gamma}{\Delta[0...N]} \mid \frac{\Delta^M\gamma}{\Delta[0..M]} \right\rangle \;=\; -\sum_{n'=0}^{N}\sum_{n=0}^{M} \frac{\Delta G/\Delta[n'n]}{\prod_{m'=0,\neq n'}^{N}(\varepsilon_{n'} - \varepsilon_{m'})\prod_{m=0,\neq n}^{M}(\varepsilon_n - \varepsilon_m)}.$$

It can be shown that this double-sum is simply the $(N+M+1)$st *Hermite divided difference* $\Delta^{M+N+1}G/\Delta[[0..M]\,N]$ of the Green matrix [5]. $\Delta^{M+N+1}G/\Delta[[0..M]\,N]$ is defined as the (M+N+1)st derivative of that polynomial of degree M+N+1 which takes the values $G(\epsilon_0), ..., G(\epsilon_N)$ at the N+1 mesh points and the energy-derivative values $\dot{G}(\epsilon_0), .., \dot{G}(\epsilon_M)$ at the first M+1 points. The single-sum expressions for the relevant cases $M = N-1$ and $M = N$ are respectively

$$\frac{\Delta^{2N}G}{\Delta[[0..N-1]\,N]} \;=\; \sum_{n=0}^{N-1} \frac{\dot{G}(\epsilon_n) - G(\epsilon_n)\left(\sum_{n'=0,\neq n}^{N-1}\frac{2}{\epsilon_n - \epsilon_{n'}} + \frac{1}{\epsilon_n - \epsilon_N}\right)}{(\epsilon_n - \epsilon_N)\prod_{m=0,\neq n}^{N-1}(\epsilon_n - \epsilon_m)^2} + \frac{G(\epsilon_N)}{\prod_{m=0}^{N-1}(\epsilon_N - \epsilon_m)^2} \tag{54}$$

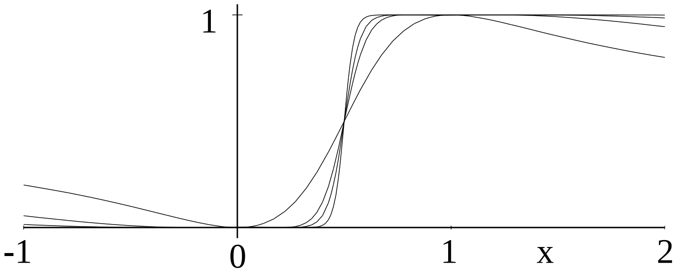

Figure 7: Variational energy-estimates for a two-level model ($\varepsilon_j = 0, 1$) using single NMTOs with $N = 0, 1, 2,$ and 4 as functions of the position x of the center of the energy mesh. For $N > 0$, the mesh is: $\epsilon_n = x - 0.2 + 0.4n/N$.

and

$$\frac{\Delta^{2N+1}G}{\Delta\left[\left[0...N\right]\right]} = \sum_{n=0}^{N} \frac{\dot{G}\left(\epsilon_n\right) - G\left(\epsilon_n\right)\sum_{n'=0,\neq n}^{N}\frac{2}{\epsilon_n - \epsilon_{n'}}}{\prod_{m=0,\neq n}^{N}\left(\epsilon_n - \epsilon_m\right)^2}. \tag{55}$$

For the overlap and Hamiltonian matrices we thus obtain the most important result [15]:

$$\begin{aligned} \left\langle \frac{\Delta^N\gamma}{\Delta\left[0..N\right]} \left|\mathcal{H} - \varepsilon\right| \frac{\Delta^N\gamma}{\Delta\left[0..N\right]} \right\rangle &= \frac{\Delta^N G}{\Delta\left[0..N\right]} \left\langle \chi^{(N)} \left|\mathcal{H} - \varepsilon\right| \chi^{(N)} \right\rangle \frac{\Delta^N G}{\Delta\left[0..N\right]} \\ &= \frac{-\Delta^{2N}G}{\Delta\left[\left[0.N-1\right]N\right]} - \left(\varepsilon - \epsilon_N\right)\frac{-\Delta^{2N+1}G}{\Delta\left[\left[0..N\right]\right]} \end{aligned} \tag{56}$$

This expression for the NMTO Hamiltonian and overlap matrices is not only simple and beautiful, but it also offers sweet coding and speedy computation. We realize that in the formalism of the 3rd-generation MTO, all relevant quantities are expressed in terms of *one* matrix, $G\left(\varepsilon\right) = \left\langle \chi^{(0)} \left|\varepsilon - \mathcal{H}\right| \chi^{(0)} \right\rangle^{-1} = K\left(\varepsilon\right)^{-1}$. We have thus derived orbital sets exclusively from multiple-scattering theory for MT-potentials.

At first glance on (56), it seems strange that the eigenvalues ε_i appear as 'ratios' of energy derivatives of Hermite interpolations of the Green matrix, which has poles inside the mesh. One might have felt more comfortable about interpolating the kink matrix. To develop some feeling for expression (56), let us first consider the simplest possible 1×1 Green matrix, $G\left(\varepsilon\right) = \sum_j \left(\varepsilon - \varepsilon_j\right)^{-1}$, which is that of a single, normalized kinked partial wave with principal quantum numbers j. The variational energy relatively to ϵ_N can easily be worked out as [5]:

$$\frac{\Delta^{2N}G/\Delta\left[\left[0..N-1\right]N\right]}{\Delta^{2N+1}G/\Delta\left[\left[0...N\right]\right]} = \frac{\sum_j \left(\varepsilon_i - \epsilon_N\right)^{-1}\prod_{n=0}^{N-1}\left(\varepsilon_j - \epsilon_n\right)^{-2}}{\sum_j \prod_{n=0}^{N}\left(\varepsilon_j - \epsilon_n\right)^{-2}}$$

and the deviation from the exact result, $\varepsilon_i - \epsilon_N$, is therefore, to leading order, $\sum_{j\neq i}\left(\varepsilon_j - \epsilon_N\right) \times \prod_{n=0}^{N}\left(\varepsilon_i - \epsilon_n\right)^2 / \left(\varepsilon_j - \epsilon_n\right)^2$. This is in accord with the opening statement of this section, that the energies have errors proportional to $\left(\varepsilon_i - \epsilon_0\right)^2 ... \left(\varepsilon_i - \epsilon_N\right)^2$. Fig. 7 shows how for the two-level system, $G\left(\varepsilon\right) = \frac{1}{\varepsilon} + \frac{1}{\varepsilon - 1}$, this variational energy switches between the exact eigenvalues 0 and 1 as the centre x of the mesh sweeps from –1 to +2. The various curves refer to $N = 0, 1, 2,$ and 4. For $N > 0$, we used meshes of total width 0.4. We see that the switching curves sharpen up as N increases, and that good results are obtained already with $N = 1$, the so-called chord-LMTO.

As another example, let us work out the expressions for the LMTO Hamiltonian and overlap matrices in terms of the kink matrix which, according to (37), is essentially the first-order two-centre Hamiltonian. The results obtained from (54)-(56) are:

$$\begin{aligned}
\left\langle \chi^{(1)} \left| \mathcal{H} - \varepsilon_1 \right| \chi^{(1)} \right\rangle &= -\left[\frac{\Delta G}{\Delta\left[01\right]} \right]^{-1} \frac{\Delta^2 G}{\Delta\left[\left[0\right]1\right]} \left[\frac{\Delta G}{\Delta\left[01\right]} \right]^{-1} \\
&= \left(\epsilon_0 - \epsilon_1\right) \left(G_0 - G_0\right)^{-1} \left(-\dot{G}_0 + \Delta G / \Delta\left[01\right] \right) \left(G_0 - G_1\right)^{-1} \\
&\rightarrow \quad -\dot{G}^{-1} \frac{\ddot{G}}{2!} \dot{G}^{-1} \; = \; -K + K \dot{K}^{-1} \frac{\ddot{K}}{2!} \dot{K}^{-1} K,
\end{aligned}$$

with $G_n \equiv G\left(\epsilon_n\right)$, and

$$\begin{aligned}
\left\langle \chi^{(1)} \mid \chi^{(1)} \right\rangle &= -\left[\frac{\Delta G}{\Delta\left[01\right]} \right]^{-1} \frac{\Delta^3 G}{\Delta\left[\left[01\right]\right]} \left[\frac{\Delta G}{\Delta\left[01\right]} \right]^{-1} \\
&= \left(G_0 - G_1\right)^{-1} \left(-\dot{G}_0 + 2\Delta G / \Delta\left[01\right] - \dot{G}_1 \right) \left(G_0 - G_1\right)^{-1} \\
&\rightarrow \quad -\dot{G}^{-1} \frac{\dddot{G}}{3!} \dot{G}^{-1} \; = \; \dot{K} - K \dot{K}^{-1} \frac{\ddot{K}}{2!} - \frac{\ddot{K}}{2!} \dot{K}^{-1} K + K \dot{K}^{-1} \frac{\dddot{K}}{3!} \dot{K}^{-1} K.
\end{aligned}$$

The results for a condensed mesh in terms of the kink matrix and its first three energy derivatives may be recognized as almost identical to those of the 2nd-generation LMTO-ASA method. To get exactly to this LMTO-ASA form, one needs to transform to the nearly orthonormal LMTO set: $\hat{\chi}^{(1)}\left(\mathbf{r}\right) \equiv \chi^{(1)}\left(\mathbf{r}\right) \dot{K}^{-1/2}$, which corresponds to Löwdin orthonormalization of the 0th-order set. However, the present formalism does not require the ASA, but it holds to leading order for overlapping MT-potentials and can be generalized to an arbitrary energy mesh. This is a most crucial improvement.

For a crystal and in the **k**-representation, one may use $\Delta^N \gamma\left(\mathbf{k}, \mathbf{r}\right) / \Delta\left[0...N\right]$ as basis-set, so that inversion of $\Delta^N G / \Delta\left[0..N\right]$ is avoided. In this case, we solve the generalized eigenvalue problem

$$\left(-\frac{\Delta^{2N} G^{\alpha}\left(\mathbf{k}\right)}{\Delta\left[\left[0..N-1\right]N\right]} + \left(\varepsilon_j\left(\mathbf{k}\right) - \epsilon_N\right) \frac{\Delta^{2N+1} G^{a}\left(\mathbf{k}\right)}{\Delta\left[\left[0...N\right]\right]} \right) g_j^a\left(\mathbf{k}\right) \; = \; 0,$$

in the downfolded representation (of size A) and normalize the eigenvectors according to:

$$g_j^{a\dagger}\left(\mathbf{k}\right) \left(-\Delta^{2N+1} G^{a}\left(\mathbf{k}\right) / \Delta\left[\left[0...N\right]\right] \right) g_j^a\left(\mathbf{k}\right) = 1.$$

The wave function in the strongly localized representation (of size $B \geq A$) is then:

$$\begin{aligned}
\Psi_j\left(\mathbf{k}, \mathbf{r}\right) &= \sum_{RL \in A} \frac{\Delta^N \gamma\left(\mathbf{k}, \mathbf{r}\right)_{RL}}{\Delta\left[0..N\right]} g_{RL,j}^a\left(\mathbf{k}\right) \\
&= \sum_{RL \in B} \sum_{T} \sum_{n=0}^{N} \phi_{RL}^b\left(\epsilon_n, \mathbf{r} - \mathbf{T}\right) \, e^{i\mathbf{k}\cdot\mathbf{T}} \sum_{R'L' \in A} \frac{G_{RL,R'L'}^b\left(\epsilon_n, \mathbf{k}\right)}{\prod_{m=0,\neq n}^{N}\left(\epsilon_n - \epsilon_m\right)} g_{R'L',j}^a\left(\mathbf{k}\right) \\
&\equiv \sum_{RL \in B} \sum_{T} \sum_{n=0}^{N} \phi_{RL}^b\left(\epsilon_n, \mathbf{r} - \mathbf{T}\right) \, e^{i\mathbf{k}\cdot\mathbf{T}} \, c_{nRL,j}^b\left(\mathbf{k}\right),
\end{aligned}$$

because it may be shown that downfolding merely *truncates* the contracted Green function $\gamma\left(\varepsilon, \mathbf{r}\right)$, but leaves it otherwise unchanged. In this expression, we have been explicit about the summations and have defined an eigenvector $c_{nRL,j}^b\left(\mathbf{k}\right)$. In terms of this, the localized form of the charge density becomes

$$\begin{aligned}
\rho\left(\mathbf{r}\right) &= \sum_{RL,R'L' \in B} \sum_{T} \sum_{n,n'=0}^{N} \phi_{RL}^b\left(\epsilon_n, \mathbf{r} - \mathbf{T}\right) \, N_{n(\mathbf{R}+\mathbf{T})L,n'R'L'}^b \, \phi_{R'L'}^b\left(\epsilon_{n'}, \mathbf{r}\right) \\
&= \rho^{\psi}\left(\mathbf{r}\right) + \sum_{R \in B} \left[\rho_R^{\varphi}\left(\mathbf{r}_R\right) - \rho_R^{\varphi^{\circ}}\left(\mathbf{r}_R\right) \right],
\end{aligned}$$

where we use the forms analogous to those following (31), but with the density matrix

$$N^b_{n(\mathbf{R}+\mathbf{T})L,n'R'L'} = \sum_{\mathbf{k}j\in occ} e^{i\mathbf{k}\cdot\mathbf{T}} c^b_{nRL,j}(\mathbf{k})\, c^{b\,*}_{n'R'L',j}(\mathbf{k})\,.$$

We finally remark that *energy-dependent, linear transformation*s of the kinked partial waves: $\hat{\phi}(\varepsilon,\mathbf{r}) = \phi(\varepsilon,\mathbf{r})\,\hat{T}(\varepsilon)$ change the individual NMTOs, but not the Hilbert space spanned by them [5]. Transformation to a *nearly orthonormal* representation, defined by $\left\langle \hat{\chi}^{(N)} \mid \hat{\chi}^{(N-1)} \right\rangle = 1$, is simple because this does not require taking the square root of the overlap matrix. Moreover, in a nearly orthonormal representation, the transfer matrices are Hamiltonians, as Eq. (51) shows, and starting from such a representation, it is a simple matter to obtain a completely *orthonormal* one. This is all explained in Ref. [5].

Band structure trend in cuprates and correlation with $T_{c\,\max}$.

In this final section, we present an extended version of a recent paper [9], which demonstrates the use of the 3rd-generation MTO method to extract the materials-dependent trend relevant for high-temperature superconductivity. Other applications of this method to correlated electron systems include Refs. [16].

The mechanism of high-temperature superconductivity (HTSC) in the hole-doped cuprates remains a puzzle [17]. Many families with CuO_2-layers have been synthesized and all exhibit a phase diagram with T_c going through a maximum as a function of doping. The prevailing explanation is that at low doping, superconductivity is destroyed with rising temperature by the loss of phase coherence, and at high doping by pair-breaking [18]. For the *materials*-dependence of T_c at optimal doping, $T_{c\,\max}$, the only known but not understood systematics is that for materials with multiple CuO_2-layers, such as $HgBa_2Ca_{n-1}Cu_nO_{2n+2}$, $T_{c\,\max}$ increases with the number of layers n, until $n \sim 3$. There is little clue as to why for n fixed, $T_{c\,\max}$ depends strongly on the family, *e.g.* why for n=1, $T_{c\,\max}$ is 40 K for La_2CuO_4, 85 K for $Tl_2Ba_2CuO_6$, and 90 K for $HgBa_2CuO_4$, although the Neel temperatures are fairly similar. A wealth of structural data has been obtained, and correlations between structure and T_c have often been looked for as functions of doping, pressure, uniaxial strain, and family. However, the large number of structural and compositional parameters makes it difficult to find what besides doping controls the superconductivity. Insight was recently provided by Seo et al. [19] who grew ultrathin epitaxial $La_{1.9}Sr_{0.1}CuO_4$ films with varying degrees of strain and measured all relevant structural parameters and physical properties. For this single-layer material it was concluded that the distance between the charge reservoir and the CuO_2-plane is the key structural parameter determining the normal state and superconducting properties.

Most theories of HTSC are based on a Hubbard model with *one* Cu $d_{x^2-y^2}$-like orbital per CuO_2 unit. The one-electron part of this model is in the $\mathbf{k}$-representation:

$$\varepsilon(\mathbf{k}) = -2t(\cos k_x + \cos k_y) + 4t' \cos k_x \cos k_y - 2t''(\cos 2k_x + \cos 2k_y) + \ldots, \tag{57}$$

with t, t', t'', ... denoting the hopping integrals (≥ 0) on the square lattice (Fig. 8). First, only t was taken into account, but the consistent results of LDA band-structure calculations [20]

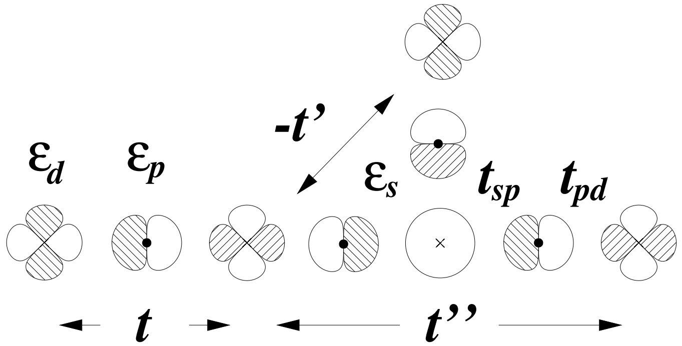

Figure 8: Relation between the one-orbital model $(t, t', t'', ...)$ and the nearest-neighbor four-orbital model [20] $(\varepsilon_d - \varepsilon_p \sim 1\,\mathrm{eV},\ t_{pd} \sim 1.5\,\mathrm{eV},\ \varepsilon_s - \varepsilon_p \sim 16 - 4\,\mathrm{eV},\ t_{sp} \sim 2\,\mathrm{eV})$.

and angle-resolved photoemission spectroscopy (for overdoped, stripe-free materials)[21], have led to the current usage of including also t', with $t'/t \sim 0.1$ for La_2CuO_4 and $t'/t \sim 0.3$ for $YBa_2Cu_3O_7$ and $Bi_2Sr_2CaCu_2O_8$, whereby the constant-energy contours of expression (57) become rounded squares oriented in respectively the [11]- and [10]-directions. It is conceivable that the materials-dependence enters the Hamiltonian primarily via its one-electron part (57), and that this dependence is captured by LDA calculations. But it needs to be filtered out:

The LDA band structure of the best known, and only stoichiometric optimally doped HTSC, $YBa_2Cu_3O_7$, is more complicated than what can be described with the t-t' model. Nevertheless, careful analysis has shown [20] that the *low*-energy *layer*-related features, which are the only generic ones, can be described by a *nearest*-neighbor, tight-binding model with *four* orbitals per layer (Fig. 8), Cu $3d_{x^2-y^2}$, $O_a\,2p_x$, $O_b\,2p_y$, and Cu $4s$, with the interlayer hopping proceeding via the diffuse Cu $4s$-orbital whose energy, ε_s, is several eV above the conduction band. Also the intralayer hoppings t', t'', ... beyond nearest neighbors in (57) proceed via Cu $4s$. The constant-energy contours, $\varepsilon_i(\mathbf{k}) = \varepsilon$, of the tight-binding model in Fig. 8 could be expressed simply as [20]:

$$1 - u - d(\varepsilon) + (1+u)\,p(\varepsilon) \;=\; \frac{v^2}{1 - u + s(\varepsilon)} \tag{58}$$

in terms of the coordinates $u \equiv \frac{1}{2}(\cos k_x + \cos k_y)$ and $v \equiv \frac{1}{2}(\cos k_x - \cos k_y)$, and the quadratic functions

$$d(\varepsilon) \equiv \frac{(\varepsilon - \varepsilon_d)(\varepsilon - \varepsilon_p)}{4t_{pd}^2} \quad \text{and} \quad s(\varepsilon) \equiv \frac{(\varepsilon_s - \varepsilon)(\varepsilon - \varepsilon_p)}{4t_{sp}^2},$$

which describe the coupling of $O_{a/b}\,p_{x/y}$ to respectively $\mathrm{Cu}\,d_{x^2-y^2}$ and $\mathrm{Cu}\,s$. The term proportional to $p(\varepsilon)$ in (58) describes the admixture of $O_{a/b}\,p_z$ orbitals for dimpled layers and actually extends the four-orbital model to a six-orbital one [20]. For ε near the middle of the conduction band, $d(\varepsilon)$, $s(\varepsilon)$, and $p(\varepsilon)$ are positive and the energy dependence of $d(\varepsilon)$ may be linearized ($\dot{d} > 0$), while that of $s(\varepsilon)$ and of $p(\varepsilon)$ may be neglected. $p = 0$ for flat layers and $p = s^2/(1+s)^2$ for extended saddlepoints. The bilayer bonding and antibonding subbands have ε_s-values split by $\mp t_{ss}^{\perp}$. Now, if ε_s were infinitely far above the conduction band, or t_{sp} were vanishingly small, the right-hand side of (58) would vanish, with the result that the constant-energy contours would depend only on u. The dispersion of the conduction band near the Fermi level would thus be that of the one-orbital model (57) with $t = (1-p)/4\dot{d}$ and $t' = t'' = 0$.

For realistic values of ε_s and t_{sp}, the conduction band attains Cu s-character proportional to v^2, thus vanishing along the nodal direction, $k_x = k_y$, and peaking at $(\pi, 0)$, where it is of order 10 per cent. The repulsion from the Cu s-band lowers the energy of the van Hove singularities and turns the constant-energy contours towards [10]-direction. This same v^2-dependence pertains to the interlayer splitting caused by $t_{ss}^{\perp}$ in a multilayer material. In order to go from (58) to (57),

$$\frac{1}{1-u+s} = \frac{2r}{1-2ru}, \quad \text{with} \quad r \equiv \frac{1/2}{1+s}, \tag{59}$$

was expanded in powers of $2ru$. This provided explicit expressions such as:

$$t = [1-p+o(r)]/4\dot{d}, \qquad t' = [r+o(r)]/4\dot{d}, \qquad \text{and} \quad t'' = \frac{1}{2}t' + o(r),$$

for the hopping integrals of the one-orbital model in terms of the parameters of the four(six)-orbital model and the expansion energy $\sim \varepsilon_F$. Note that all intralayer hoppings beyond nearest neighbors are expressed in terms of the *range*-parameter r. Although one may think of r as t'/t, this holds only for flat layers and when $r < 0.2$. When $r > 0.2$, the series (57) must be carried beyond t''. Dimpling is seen not to influence the range of the intralayer hopping, but to reduce t through admixture of $\mathrm{O}_{a/b}\, p_z$. In addition, it reduces t_{pd}.

We shall now generalize this analysis to all known families of HTSC materials using the 3rd-generation MTO method which allows us to construct *minimal basis sets* for the *low-energy part* of an LDA band structure with sufficient accuracy that we can extract the materials dependence. This dependence we find to be contained solely in ε_s, which is now the energy of the *axial* orbital, a hybrid between Cu s, Cu d_{3z^2-1}, apical-oxygen $\mathrm{O}_c\, p_z$, and farther orbitals on *e.g.* La or Hg. The range, r, of the intralayer hopping is thus controlled by the structure and chemical composition *perpendicular* to the CuO$_2$-layers. It turns out that the materials with the larger r (lower ε_s) tend to be those with the higher observed values of $T_{c\,\max}$. In the materials with the highest $T_{c\,\max}$, the axial orbital is almost pure Cu $4s$.

It should be noted that r describes the *shape* of the non-interacting band in a 1 eV-range around the Fermi level, whose accurate position is unknown because we make no assumptions about the remaining terms of the Hamiltonian, inhomogeneities, stripes, a.s.o.

The top of Fig. 9 shows the LDA energy bands calculated for the simplest, idealized, infinite-layer cuprate, CaCuO$_2$. The red conduction band was obtained using a single Bloch-sum of the Cu $d_{x^2-y^2}$ (N=4)MTO, which is shown in the CuO$_2$-layer in the bottom part of the figure. All other channels were downfolded. We see the central Cu $3d_{x^2-y^2}$-orbital, surrounded by four O $2p$-orbitals anti-bonding to it. At the four next Cu sites there is substantial diffuse Cu $4s$-character bonding to O $2p$. This character is best recognized as a strengthening of the O $2p$ back-lobes followed by sharp truncation at the outermost node of the Cu $4s$ orbital. Having understood these general in-layer features, we now consider the real materials:

Fig. 10 shows the LDA bands for the single-layer La$_2$CuO$_4$ and Tl$_2$Ba$_2$CuO$_6$. Whereas the high-energy band structures are complicated and very different, the low-energy conduction bands shown by dashed lines contain the generic features. Most notably, the dispersion along ΓDZ is suppressed for Tl$_2$Ba$_2$CuO$_6$ relatively to La$_2$CuO$_4$, whereas the dispersion along ΓXZ is the same. This is the v^2-effect. The low-energy bands were calculated using the first-order tight-binding Hamiltonian (38) with a single Bloch sum of Cu $d_{x^2-y^2}$-KPWs, or (N=0)MTOs, with ϵ_0

CaCuO_2(flat)

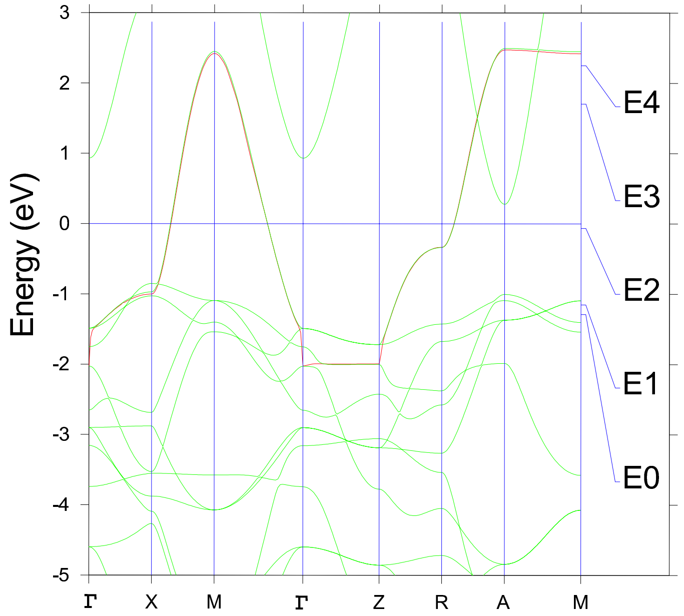

(N=4) MTO

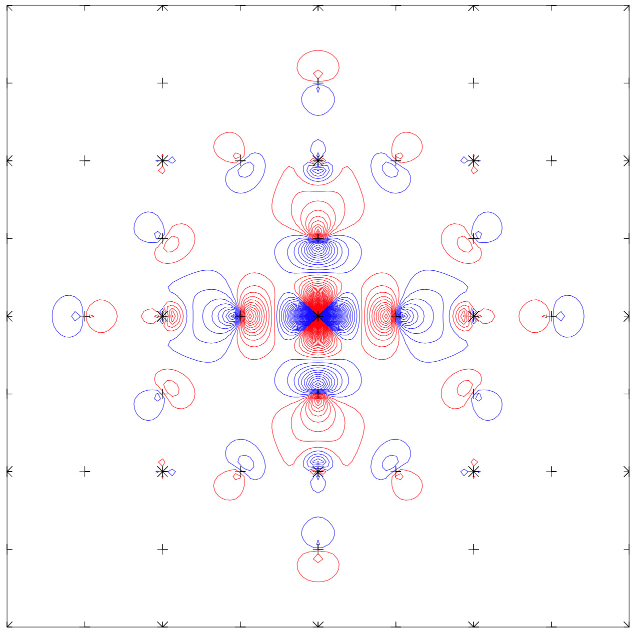

Figure 9: LDA energy bands of idealized $CaCuO_2$ with flat CuO_2-layers. The red band was obtained using the Cu $d_{x^2-y^2}$ MTO shown in the CuO_2-layer in the bottom part of the figure.

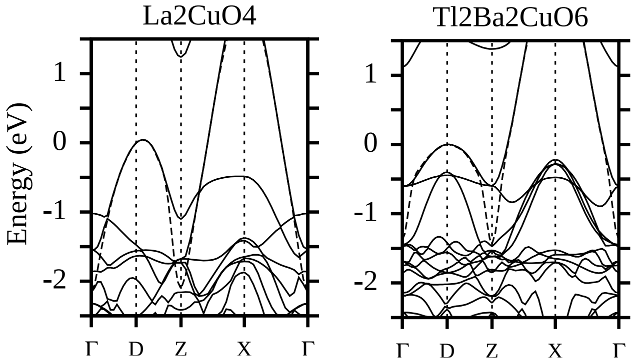

Figure 10: LDA bands calculated with the NMTO method in the bct structure. The dashed band was obtained using the Bloch sum of MTOs with N=0 and Cu $d_{x^2-y^2}$ symmetry at the central site. $\Gamma\ (0,0,0)$, D $(\pi,0,0)$, Z $(2\pi,0,0)=(0,0,2\pi/c)$, X $(\pi,\pi,0)$.

near half-filling. The low-energy bands agree with the full band structures to linear order and, in contrast to the N=4-bands in Fig. 9, head smoothly towards the pure Cu $d_{x^2-y^2}$-levels at Γ and Z, extrapolating across a multitude of other bands. Now, the hopping integrals t, t', t'',.... may be obtained by expanding the low-energy band as a Fourier series. This yields: $t=0.43\,\mathrm{eV}$ in both cases, $t'/t=0.17$ for La_2CuO_4 and 0.33 for $Tl_2Ba_2CuO_6$, and also many further inter- and intralayer hopping integrals [22].

That all these hopping integrals and their materials-dependence can be described with a generalized four-orbital model is conceivable from the appearance of the conduction-band orbital for La_2CuO_4 shown in Fig. 11 in the xz-plane perpendicular to the layer. Starting from the central Cu atom and going in the x-direction, we see $3d_{x^2-y^2}$ antibond to neighboring $O_a\ 2p_x$, which itself bonds to 4s and antibonds to $3d_{3z^2-1}$ on the next Cu. From here, and in the z-direction, we see 4s and $3d_{3z^2-1}$ antibond to $O_c\,2p_z$, which itself bonds to La orbitals, mostly $5d_{3z^2-1}$. In the y-direction, 4s antibonds and $3d_{3z^2-1}$ bonds to $O_b\,2p_y$. For the 85 K superconductor $Tl_2Ba_2CuO_6$, we find about the same amount of Cu $3d_{x^2-y^2}$ and $O_{a/b}\,2p_{x/y}$ character, but more Cu 4s, negligible Cu $3d_{3z^2-1}$, much less $O_c\,2p_z$, and Tl 6s instead of La $5d_{3z^2-1}$ character. That is, in $Tl_2Ba_2CuO_6$ the axial part is mainly Cu 4s. The situation is essentially the same in the simple tetragonal 90 K superconductor $HgBa_2CuO_4$. This is seen in Fig. 12: there is essentially no apical-oxygen character, but substantial Cu 4s as recognized from the node it cuts in the plane-oxygen orbital.

Calculations with larger basis sets than one MTO per CuO_2 now confirm that, in order to localize the orbitals to the extent that only nearest-neighbor hoppings are essential, one needs to add *one* orbital, Cu axial, to the three standard ones [22]. This axial (N=0)MTO obtained from calculations with Cu $d_{x^2-y^2}$, $O_a\ p_x$, $O_b\ p_y$, and Cu s chosen as active is shown in Fig. 13 for $HgBa_2CuO_4$ (left) and La_2CuO_4 (right). The corresponding four-orbital Hamiltonian is therefore the one described above in Fig. 8 and in Eqs. (58)-(59). Note that we continue to call the energy of the axial orbital ε_s, and its hopping integral with $O_{a/b}\,p_{x/y}$ for t_{sp}. Calculations with this basis set for many different materials show that, of all the parameters, only ε_s varies significantly [22]. This variation can be understood in terms of the couplings between the constituents of the axial orbital sketched in the right-hand panel of Fig. 11: We first form the

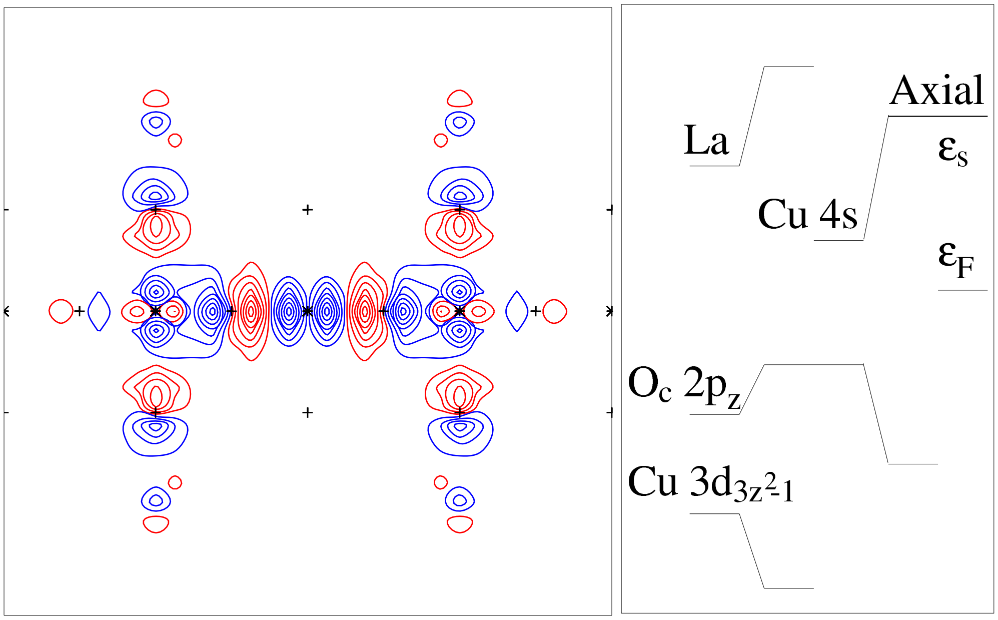

Figure 11: *Left:* N=0 MTO describing the Cu $d_{x^2-y^2}$-like conduction band in La_2CuO_4. The plane is perpendicular to the layers and passes through Cu, O_a, O_c, and La. *Right:* Schematic diagram giving the energy ε_s of the *axial* orbital in terms of the energies of its constituents and their couplings.

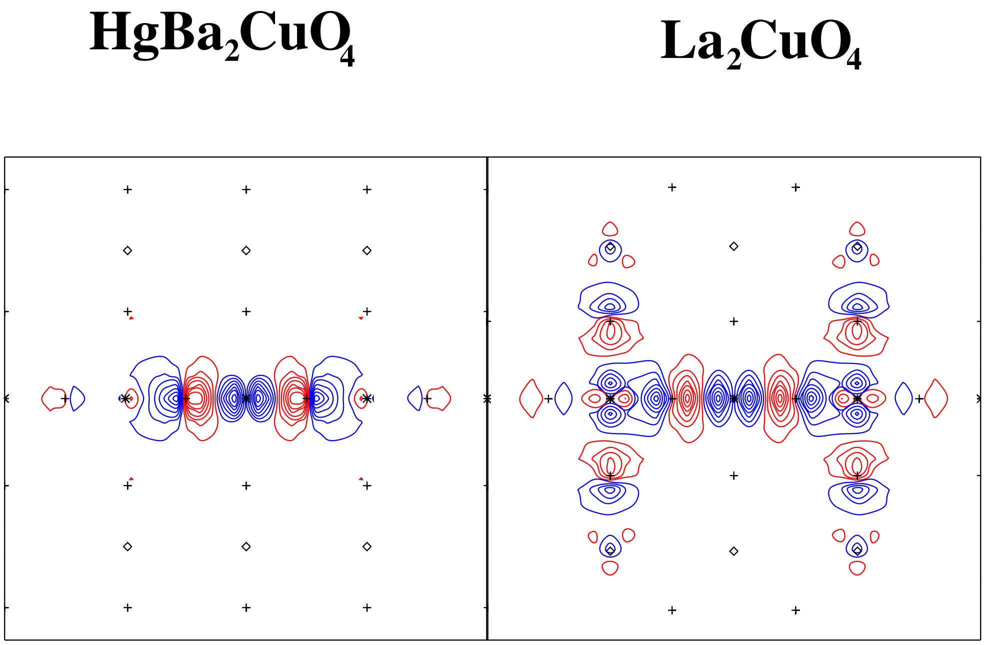

Figure 12: As left-hand side of Fig. 11 and including the conduction-band orbital for $HgBa_2CuO_4$.

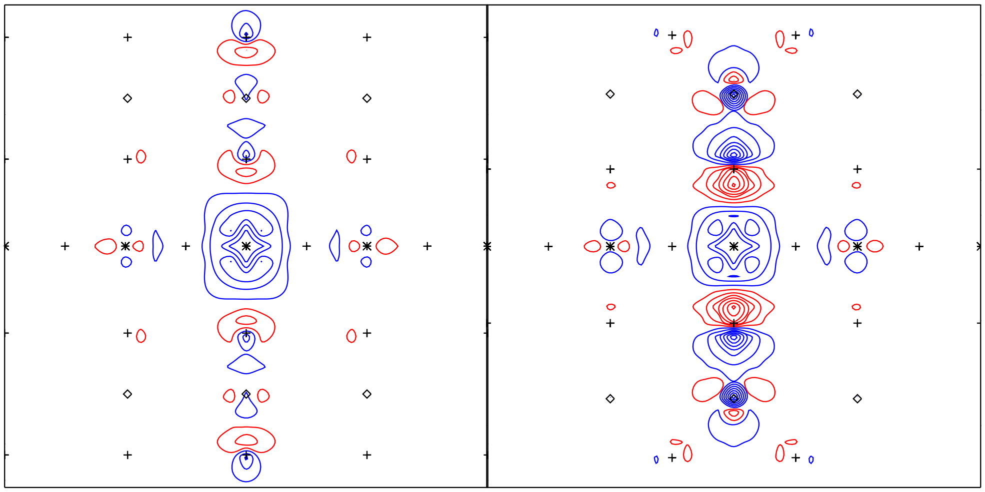

Figure 13: Axial orbital (KPW) for $HgBa_2CuO_4$ (left) and La_2CuO_4 (right) in the xz-plane perpendicular to the CuO_2 layer.

appropriate $\mathrm{O}_c\,p_z$-like 5-atom hybrid $\mathrm{Cu}\,d_{3z^2-1}$ - $2\mathrm{O}_c\,p_z$ - $2\,\mathrm{La}$ with the energy [22]

$$\varepsilon_c = \varepsilon_{\bar{c}} + \left(1 + \frac{t_{sc}}{t_{sp}}\frac{t_{pz^2}}{t_{cz^2}}\right)^2 \frac{4\bar{r}t_{cz^2}^2}{\varepsilon_F - \varepsilon_{z^2}} - \frac{t_{c\,La}^2}{\varepsilon_{La} - \varepsilon_F}, \qquad (60)$$

and then we couple this to the $\mathrm{Cu}\,s$-orbital to yield the energy

$$\varepsilon_s = \varepsilon_{\bar{s}} + \frac{2t_{sc}^2}{\varepsilon_F - \varepsilon_c}$$

of the axial orbital. Here, the energies of the pure $\mathrm{Cu}\,s$- and $\mathrm{O}_c\,p_z$-orbitals are denoted $\varepsilon_{\bar{s}}$ and $\varepsilon_{\bar{c}}$, respectively, while their hopping integral is t_{sc}. The energy of the Cu d_{3z^2-1}-orbital is ε_{z^2} and its hopping integrals to $\mathrm{O}_{a/b}\,p_{x/y}$ and $\mathrm{O}_c\,p_z$ are respectively t_{pz^2} and t_{cz^2}. In deriving [22] Eqs. (58)-(60), we have exploited that

$$\frac{t_{pz^2}^2}{t_{sp}^2} \ll \frac{\varepsilon_F - \varepsilon_{z^2}}{\varepsilon_{\bar{s}} - \varepsilon_F} \qquad \text{and} \qquad \frac{t_{pd}^2}{t_{sp}^2} \ll \frac{\varepsilon_F - (\varepsilon_p + \varepsilon_d)/2}{\varepsilon_F - (\varepsilon_p + \varepsilon_s)/2}.$$

Although specific for La_2CuO_4, Eq. (60) is easy to generalize.

In Fig. 14 we plot the r-values for single-layer materials against the distance $d_{\mathrm{Cu-O}_c}$ between Cu and apical oxygen. r increases with $d_{\mathrm{Cu-O}_c}$ because ε_s is lowered towards ε_F when the coupling between $\mathrm{O}_c\,p_z$ and $\mathrm{Cu}\,d_{3z^2-1}/s$ is weakened. Since $t_{cz^2} \propto d_{\mathrm{Cu-O}_c}^{-4}$ and $t_{sc} \propto d_{\mathrm{Cu-O}_c}^{-2}$, increasing the distance suppresses the $\mathrm{Cu}\,d_{3z^2-1}$ content, which is then important in La_2CuO_4, but negligible in $Tl_2Ba_2CuO_6$ and $HgBa_2CuO_4$. This is also reflected in the slopes of the lines in Fig. 14 which give r vs. $d_{\mathrm{Cu-O}_c}$ for each material. The strong slope for La_2CuO_4 explains the findings of Seo *et al.* [19], provided that r correlates with superconductivity. That the Bi-point does not fall on the La-line is an effect of Bi being different from La: $\mathrm{Bi}\,6p_z$ couples stronger to $\mathrm{O}_c\,2p_z$ than does $\mathrm{La}\,5d_{3z^2-1}$. The figure shows that upon reaching $HgBa_2CuO_4$, r is saturated, $\varepsilon_s \sim \varepsilon_{\bar{s}}$, and the axial orbital is almost purely $\mathrm{Cu}\,4s$.

Fig. 14 hints that for single-layer materials r might correlate with the observed $T_{c\,\max}$. But the experimental uncertainties of both $T_{c\,\max}$ and the structural parameters are such that we

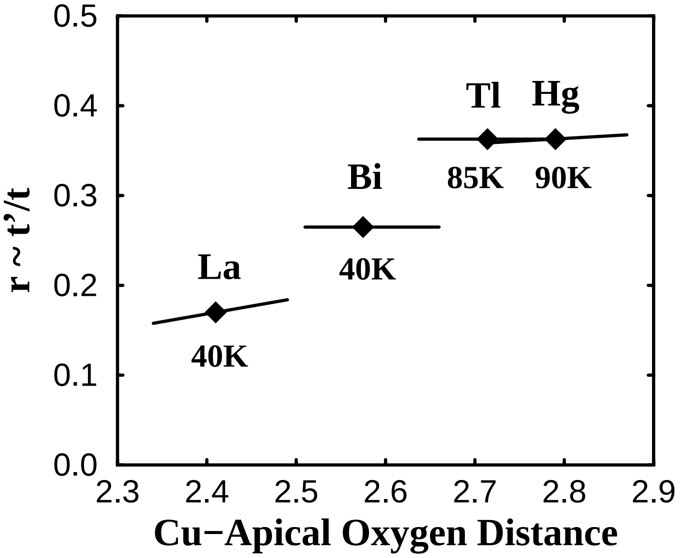

Figure 14: Calculated range parameter, r, for single-layer materials vs. the distance (in Å) between Cu and O_c. The lines result from rigid displacements of O_c.

need better statistics. Therefore, we plot the observed $T_{c\,\max}$ against the calculated r-values for 15 different HTSC families in Fig. 15. For the single-layer materials we observe a strong correlation between r and $T_{c\,\max}$, which seems to be continued in the *bonding* subband for the multilayer materials (filled squares). This indicates that the electrons are delocalized over the multilayer [25], and that $T_{c\,\max}$ increases with the number of layers for the *same* reason that it increases among single-layer materials; the multilayer is simply a means of lowering ε_s further, through the formation of Cu $4s$-Cu $4s$ bonding states. This is consistent with the celebrated pressure-enhancement [24] of T_c in $\mathrm{HgBa_2Ca_2Cu_3O_8}$. One might attempt to increase $T_{c\,\max}$, say for $\mathrm{YBa_2Cu_3O_7}$, by substituting Y with a smaller cation, *e.g.* Sc. This has not been done, but a *larger* cation, La, was recently inserted [23] and caused $T_{c\,\max}$ to drop from 92 K to 50 K. Using the observed structure of $\mathrm{LaBa_2Cu_3O_7}$, we have calculated the r-values and included them in Fig. 15. Here again, the bonding subband is seen to follow the trend! That $T_{c\,\max}$ eventually drops for an increasing number of layers, is presumably caused by loss of phase coherence.

Interlayer coupling in bct $\mathrm{La_2CuO_4}$ mainly proceeds by hopping from $\mathrm{O}_c\,p_z$ at $(0,0,zc)$ to its four nearest neighbors at $\left(\pm\frac{1}{2},\pm\frac{1}{2},\left(\frac{1}{2}-z\right)c\right)$, and is therefore taken into account by adding to $\varepsilon_{\bar{c}}$ on the right-hand side of (60) the term

$$-8t_{cc}^{\perp}\cos\frac{1}{2}k_x\cos\frac{1}{2}k_y\cos\frac{1}{2}ck_z.$$

In primitive tetragonal materials, the corresponding term is merely proportional to $\cos ck_z$ because the $\mathrm{CuO_2}$-layers are stacked on top of each other, *e.g.* in $\mathrm{HgBa_2CuO_4}$, the interlayer coupling proceeds from $\mathrm{O}_c\,p_z$ at $(0,0,zc)$ via Hg $6s/6p_z$ at $(0,0,c/2)$ to $\mathrm{O}_c\,p_z$ at $(0,0,(1-z)\,c)$. Periodic interlayer coupling thus makes ε_s depend on k_z, and this passes onto the conduction band a k_z-dispersion proportional to $v^2\cos\frac{1}{2}k_x\cos\frac{1}{2}k_y\cos\frac{1}{2}ck_z$ in bct, and to $v^2\cos ck_z$ in tetragonal structures. Fig. 15 shows how the k_z-dispersion of r decreases with contraction of the axial orbital onto the (multi)layer.

Our identification of an electronic parameter, r or ε_s, which correlates with the observed $T_{c\,\max}$

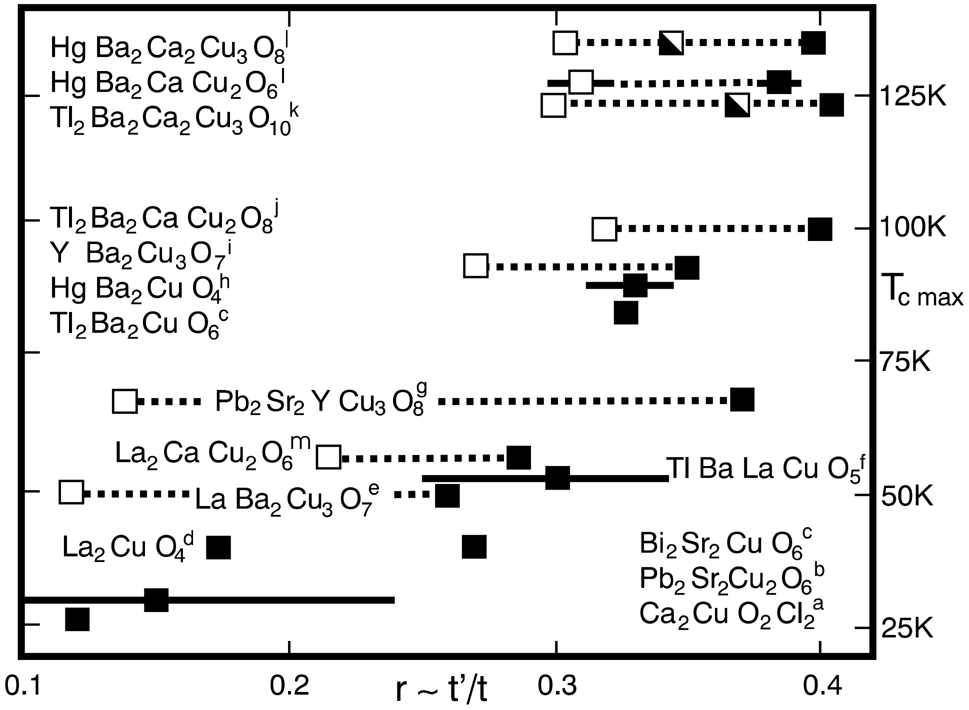

Figure 15: Correlation between calculated r and observed $T_{c\,\max}$. *Filled squares:* Single-layer materials and most bonding subband for multilayers. *Empty squares:* Most antibonding subband. *Half-filled squares:* Non-bonding subband. *Dotted lines* connect subband-values. *Bars* give k_z-dispersion of r in primitive tetragonal materials.

for all known types of hole-doped HTSC materials should be a useful guide for materials synthesis and a key to understanding the mechanism of HTSC. With current **k**-space renormalization-group methods one could for instance investigate the effect of the band shape on the leading correlation-driven instabilities [26]. Moreover, the possibility that a longer hopping-range leads to better screening of the Coulomb repulsion, maybe even to overscreening, could be studied. Increased diagonal hopping t' might lead to higher $T_{c\,\max}$ by suppression of static stripe order [27]. The Van Hove scenario [28] finds no support in Fig. 15 because it is the saddlepoint of the *anti*-bonding band which is at the LDA Fermi level in $\mathrm{YBa_2Cu_3O_7}$; the bonding band is about half-filled and enhances spin-fluctuations with $\mathbf{q} \approx (\pi, \pi)$ [29]. The propensity to buckling is increased by pushing the conduction band towards the $\mathrm{O}_{a/b}\, p_z$-level [20] by lowering of ε_s, but recent structural studies [23] as well as Fig. 15 disprove that static buckling enhances $T_{c\,\max}$, although dynamical buckling might. The interlayer-pair-tunnelling mechanism [30] is ruled out by the fact that the additional factor $\cos \frac{1}{2}k_x \cos \frac{1}{2}k_y$ attained by $t^{\perp}(\mathbf{k})$ in bct materials suppresses the interlayer pair-tunnelling in $\mathrm{Tl_2Ba_2CuO_6}$ compared with $\mathrm{HgBa_2CuO_4}$, and yet, $T_{c\,\max} \sim 90\,\mathrm{K}$ in both cases. That the axial orbital is *the* channel for coupling the layer to its surroundings is supported [31] by the observations that the **k**-dependence of the scattering in the normal state is v^2-like [21] and that the c-axis transport is strongly suppressed by the opening of a pseudogap [32] with similar **k**-dependence. The axial orbital is also *the* non-correlated vehicle for coupling between oxygens in the layer. Therefore it seems plausible that contraction of the axial orbital around the $\mathrm{CuO_2}$-layer, away from the non-stoichiometric layers, will strengthen the phase coherence and thus increase $T_{c\,\max}$. Thermal excitation of nodal quasiparticles [33] is, on the other hand, hardly the mechanism by which the superconducting state is destroyed, because the axial orbital does not influence the band in the nodal direction.

Finally we note that the correlation between r and $T_{c\,\max}$ does not extend to electron-doped cuprates, where the mechanism for superconductivity thus seems to be different.

Conclusion

We have solved the long-standing problem [34] of deriving energy-independent, short-ranged orbitals from scattering theory. What in the 1st-generation of the LMTO formalism was possible only through the Ansatz of neglecting the energy dependence in the interstitial, was solved in the 2nd and 3rd generations through an exact screening transformation. By treating the interstitial on the same footing as the MT-spheres, the direct relation to scattering theory, efficient downfolding through screening, and the extension to overlapping, but short-ranged potentials comes 'for free.' However, since the energy ϵ_0 around which the partial waves are expanded is now global, Taylor expansion to linear order is not always sufficient. The final step was therefore to generalize to arbitrary order and discrete meshes. By application of the NMTO formalism to a few examples, we hope to have indicated how it may become of considerable practical importance.

References

[1] J. Korringa, Physica **13,** 392 (1947); W. Kohn and J. Rostoker, Phys. Rev. **94,** 1111 (1954).

[2] O.K. Andersen, O. Jepsen, and G. Krier in *Lectures on Methods of Electronic Structure Calculations,* edited by V. Kumar, O.K. Andersen, and A. Mookerjee (World Scientific Publishing Co., Singapore, 1994), pp. 63-124.

[3] O.K. Andersen, C. Arcangeli, R.W. Tank, T. Saha-Dasgupta, G. Krier, O. Jepsen, and I. Dasgupta in *Tight-Binding Approach to Computational Materials Science,* Eds. L. Colombo, A. Gonis, P. Turchi, Mat. Res. Soc. Symp. Proc. Vol. 491 (Materials Research Society, Pittsburgh, 1998) pp 3-34.

[4] R.W. Tank and C. Arcangeli, phys. stat. sol. (b) **217**, 89-130 (2000).

[5] O.K. Andersen, T. Saha-Dasgupta, R.W. Tank, C. Arcangeli, O. Jepsen, and G. Krier in *Electronic Structure and Physical Properties of Solids. The Uses of the LMTO Method,* Ed. H. Dreysse (Springer Lecture Notes in Physics, New York, 2000) pp. 3-84.

[6] O.K. Andersen and C. Arcangeli (unpublished); C. Arcangeli and O.K. Andersen (unpublished).

[7] D. Savrasov and O.K. Andersen (unpublished).

[8] L. Vitos, H.L. Skriver, B. Johansson, et al., Comp. Mater. Sci. **18,** 24 (2000).

[9] Pavarini E., I. Dasgupta, T. Saha-Dasgupta, O. Jepsen, O.K. Andersen, Phys. Rev. Lett. **87**, 047003 (2001).

[10] O.K. Andersen and T. Saha-Dasgupta, Phys. Rev. B **62,** R16 219 (2000).

[11] For a review, see F. Aryasetiawan *et al.,* Rep. Prog. Phys. **61,** 237 (1998).

[12] L. Tsetseris, O. Jepsen, and O.K. Andersen (unpublished).

[13] O.K. Andersen, A.V. Postnikov, and S. Yu. Savrasov, in *Applications of Multiple Scattering Theory to Materials Science,* eds. W.H. Butler, P.H. Dederichs, A. Gonis, and R.L. Weaver, MRS Symposia Proceedings No. 253 (Materials Research Society, Pittsburgh, 1992) pp 37-70.

[14] Our energy windows are limited in size by the requirement, that for two energies within the window, $\phi_{RL}(\varepsilon, \mathbf{r})$ and $\phi_{RL}(\varepsilon', \mathbf{r})$ cannot be orthogonal. Hence, the present NMTOs do not carry principal quantum numbers.

[15] In Eq. (6) of Ref. [10], $-(\varepsilon - \epsilon_N)$ is misprinted as $+(\varepsilon - \epsilon_N)$.

[16] T.F.A. Müller *et al.,* Phys. Rev. B **57**, R12655 (1998); D.D. Sarma *et al.*, Phys. Rev. Lett. **85**, 2549 (2000); R. Valenti *et al.*, cond-mat/0101282.

[17] For a recent review, see J. Orenstein and A.J. Millis, Science **288**, 468 (2000), and further articles in that volume.

[18] V.J. Emery and S.A. Kivelson, Nature **374**, 434 (1995).

[19] J.W. Seo *et al.*, 18th EPS-CMD Conference, Montreux, p 363 (2000); J.-P. Locquet *et al.* Nature **394**, 453 (1998) and H. Sato *et al.,* Phys. Rev. **61**, 12 447 (2000).

[20] O.K. Andersen *et al.*, J. Phys. Chem. Solids **56**, 1573 (1995); J. Low. Temp. Physics **105**, 285 (1996).

[21] Z.X. Shen and D.S. Dessau, Phys. Rep **253**,1 (1995); H.H. Fretwell *et al.*, Phys. Rev. Lett. **84**, 4449 (2000); S.V. Borisenko *et al.*, Phys. Rev. Lett. **84**, 4453 (2000).

[22] I. Dasgupta *et al.* (to be published).

[23] D. Godschmidt *et al.*, Phys. Rev. B **48**, 532 (1993); O. Chmaissem *et al.*, Nature **397,** 45 (1999).

[24] C.W. Chu *et al.,* Nature **365**, 323 (1993); M. Nunez-Regueiro *et al.,* Science **262**, 97 (1993).

[25] This is consistent with the observation of bilayer splitting by D.L. Feng *et al.*, cond-mat/0102385.

[26] C.J. Halboth and W. Metzner, Phys. Rev. B **61**, 7364 (2000); C. Honerkamp *et al.,* cond-mat/9912358.

[27] M. Fleck *et al.,* cond-mat/0102041.

[28] D.M. Newns *et al.*, Com.Cond.Mat.Phys. **15,** 273 (1992).

[29] V.S. Oudovenko *et al.,* Physica C **336**, 157 (2000).

[30] S. Chakravarty *et al.,* Science **261**, 337 (1993).

[31] A.Z. Zheleznyak *et al.,* Phys.Rev. B **57**, 3089 (1998); L.B. Ioffe and A.J. Millis, Phys. Rev. B **58,** 11631 (1998).

[32] D. Basov *et al.*, Phys. Rev. B **50**, 3511 (1994); C.C. Holmes *et al.*, Physica C **254**, 265 (1995).

[33] P.A. Lee and X.G. Wen, Phys. Rev. Lett. **78**, 4111 (1997).

[34] See for instance, J. Hubbard, Proc. Phys. Soc. London. **92,** 921 (1967).